

Journal of Geophysical Research: Solid Earth

RESEARCH ARTICLE

10.1002/2014JB011455

Key Points:

- Discrete element models of fold and thrust belts resolve stress and strain
- Material cohesion determines fault types, geometries, and distributions
- Mechanical behavior correlates directly with deformation episodes

Correspondence to:

J. K. Morgan,
morgan@rice.edu

Citation:

Morgan, J. K. (2015), Effects of cohesion on the structural and mechanical evolution of fold and thrust belts and contractional wedges: Discrete element simulations, *J. Geophys. Res. Solid Earth*, 120, 3870–3896, doi:10.1002/2014JB011455.

Received 15 JUL 2014

Accepted 14 APR 2015

Accepted article online 21 APR 2015

Published online 22 MAY 2015

Effects of cohesion on the structural and mechanical evolution of fold and thrust belts and contractional wedges: Discrete element simulations

Julia K. Morgan¹

¹Department of Earth Science, Rice University, Houston, Texas, USA

Abstract Particle-based numerical simulations of cohesive contractional wedges can yield important perspectives on the formation and evolution of fold and thrust belts, offering particular insights into the mechanical evolution of the systems. Results of several discrete element method simulations are presented here, demonstrating the stress and strain evolution of systems with different initial cohesive strengths. Particle assemblages consolidated under gravity, and bonded to impart cohesion, are pushed from the left at a constant velocity above a weak, unbonded décollement surface. Internal thrusting causes horizontal shortening and vertical thickening, forming wedge geometries. The mean wedge taper is similar for all simulations, consistent with their similar residual and basal sliding friction values. In all examples presented here, both forethrusts and back thrusts occur, but forethrusts accommodate most of the shortening. Fault spacing and offset increase with increasing cohesion. Significant tectonic volume strain also occurs, with the greatest incremental volume strain occurring just outboard of the deformation front. This diffuse shortening serves to strengthen the unfaulted domain in front of the deformed wedge, preconditioning these materials for brittle (dilative) failure. The reach of this volumetric strain and extent of décollement slip increase with cohesive strength, defining the extent of stress transmission. Stress paths for elements tracked through the simulations demonstrate systematic variations in shear stress in response to episodes of both décollement slip and thrust fault activity, providing a direct explanation for stress fluctuations during convergence.

1. Introduction

Fold and thrust belts and accretionary prisms are among the most fundamental features associated with mountain building, commonly fringing the highest peaks in the world (e.g., the Himalayas), and preserving a record of past and present convergent tectonic plate motions. Fold and thrust belts often also contain rich petroleum reserves, leading to extensive investigations of their structure and evolution [Bally *et al.*, 1966; Dahlstrom, 1970; Price, 1981; Boyer and Elliott, 1982]. Field studies and geophysical surveys are the most obvious ways to constrain the internal structure of these domains, in particular for petroleum prospecting, but due to limited exposures and uncertain seismic velocity structure, the resulting observations are still commonly subject to interpretation.

The mechanical conditions under which these systems develop are also of critical importance, influencing the gross wedge geometries [Davis *et al.*, 1983; Davis and Engelder, 1985; DeCelles and Mitra, 1995; Adam and Reuther, 2000], fault spacing [Marshak and Wilkerson, 1992; Mandal *et al.*, 1997; Schott and Koyi, 2001; Agarwal and Agrawal, 2002; Bose *et al.*, 2009], and small-scale features responsible for fluid transport and storage (e.g., fracture distributions, porosity, and permeability) [e.g., Sanz *et al.*, 2008]. However, mechanical constraints are difficult to obtain in the field and are less than reliable in ancient fold and thrust belts [Gray *et al.*, 2014]. For these reasons, forward modeling approaches, both analog and numerical, are used to investigate the internal structure and evolution of fold and thrust belts and other contractional wedges around the world [e.g., Mulugeta, 1988; Willet, 1999; Stockmal *et al.*, 2007; Konstantinovskaya *et al.*, 2009; Bigi *et al.*, 2010; Simpson, 2011]. Such studies, however, often emphasize the large-scale geometric evolution of such systems, providing little insight into controlling mechanical processes. This study employs particle-based numerical methods to simulate the development of cohesive contractional wedges, in order to understand the interplay between material strength, stress evolution, and the structural evolution of these systems, at both large and small scales.

2. Background

An important conceptual breakthrough in the mechanics of fold and thrust belts and accretionary prisms arose from the appreciation that shallow Earth materials obey a frictional Coulomb rheology [Chapple, 1978]. A balance of forces across a tectonically driven wedge yields a predictable “critical taper” for a given internal and basal sliding friction [Davis *et al.*, 1983; Dahlen, 1984, 1990]. This concept has been applied to natural systems [Davis *et al.*, 1983; Lallemand *et al.*, 1994; DeCelles and Mitra, 1995; Mitra, 1997] and tested physically and numerically, where frictional properties are known a priori [e.g., Mulugeta and Koyi, 1987; Mulugeta, 1988; Koyi, 1995; Koyi and Vendeville, 2003]. However, many of these studies still focus on the mechanical controls on gross wedge geometry. Less well understood are how mechanical properties control the local structure and stress conditions within deforming contractional wedges, how these stresses vary over time and space, and how these might determine internal structure of fold and thrust belts.

Physical modeling, in particular using sand, clay, or gel as analogs for natural materials, represents a powerful tool for investigating the growth and internal structures of fold and thrust belts [Cotton and Koyi, 2000; Costa and Vendeville, 2002; Couzens-Schultz *et al.*, 2003; Lujan *et al.*, 2003; Cruz *et al.*, 2008; Duerto and McClay, 2009; Vidal-Royo and Munoz, 2009; Konstantinovskaya and Malavieille, 2011]. Different materials or material preparation allow the study of effects of lithologic variations on structural evolution [e.g., Schellart, 2000; Lohrmann *et al.*, 2005; Teixell and Koyi, 2003; Ruh *et al.*, 2012]. Physical models, however, suffer from the inability to track the full evolution of a deforming system in detail, and more importantly, an inability to monitor the specific mechanical controls on their behavior. Mechanical properties of the component materials can be derived in advance [Mulugeta, 1988; Gutscher *et al.*, 1996, 1998; Schreurs *et al.*, 2006; Bonini, 2007] and directly correlated with the resulting wedge geometries and internal structure. Direct stress measurements within deforming analog models, however, remain a challenge, although preliminary efforts using *in situ* pressure transducers demonstrate intriguing temporal stress variations, as yet incompletely understood [Nieuwland *et al.*, 2000]. External stresses, e.g., along a moving back wall, are more easily monitored, demonstrating distinct stress drops associated with fault initiation [Cruz *et al.*, 2010; Souloumiac *et al.*, 2010].

These initial analog modeling studies demonstrate the temporal and spatial heterogeneities in stress conditions and evolution but do not yet establish their correlations with structural deformation. Numerical modeling, e.g., using the finite element method, offers an alternative approach, enabling detailed stress and strain behavior of the system to be tracked [Willet, 1999; Buiter *et al.*, 2006; Stockmal *et al.*, 2007; Cruz *et al.*, 2010; Simpson, 2011]. But many such models also suffer from limited resolution, prescribed rheologies, and the assumption that the system behaves as a continuum, which tends to smooth the resulting stress and strain fields [e.g., Gray *et al.*, 2014].

Recently, particle-based numerical methods, for example, the discrete element method (DEM), have been applied to the study of fold and thrust belt deformation and evolution [Burbridge and Braun, 2002; Vietor, 2003; Strayer *et al.*, 2004; Naylor *et al.*, 2005; Buiter *et al.*, 2006; Hardy *et al.*, 2009; Miyakawa *et al.*, 2010], defining a hybrid approach that captures the discrete nature of physical sandbox models and the computational benefits of numerical models, but without the assumptions of continuity or predefined material rheologies. Instead, a range of complex interparticle contact laws can be introduced that yield realistic brittle elasto-plastic rheologies [Cundall and Strack, 1979; Mora and Place, 1993] responsible for natural structures and geometries. These studies reproduce many fundamental observations of analog sandbox models, including the formation of imbricate stacks of forethrusts, and variations in wedge taper and thrust spacing due to underlying décollement strength [e.g., Egholm *et al.*, 2007; Yamada and Matsuoka, 2005; Yamada *et al.*, 2006]. Still, most of these studies have focused on the large-scale structural evolution and kinematics of contractional systems; a few have emphasized the unique ability of DEM simulations to reveal the detailed processes of and controls on failure, fault linkage, and deformation [Schöpfer *et al.*, 2007a, 2007b; Camac *et al.*, 2009; Hardy *et al.*, 2009; Schöpfer *et al.*, 2013]. However, fewer have taken the next step of exploring the detailed mechanics of deformation within these large-scale simulations, instead using them as numerical sandboxes, even though the mechanical basis of contact interactions sets the stage quite well for more detailed analysis.

This study outlines the methodologies of our DEM approach and data analyses, and explores the detailed kinematic and mechanical evolution of homogeneous systems with different cohesive strengths, subjected

to horizontal shortening. The evolving mechanical conditions during wedge development are well resolved, and local stress conditions can be tracked during episodes of deformation, e.g., décollement slip or initiation and propagation of discrete thrust faults, clarifying the mechanical controls on deformation within these contractional systems.

3. Discrete Element Method

The discrete element method [e.g., *Cundall and Strack*, 1979] is a particle-based numerical technique that employs a time stepping, finite difference approach to solve Newton's equations of motion for every particle in a system. The method first solves for forces imposed on the surfaces of each particle by neighboring particles or boundaries and then calculates a displacement based on the acceleration caused by the sum of these forces. Particle motions are induced by gravitational forces, external forces prescribed by stress or strain rate boundary conditions, and by forces resolved at interparticle contacts. The disequilibrium of forces drives particle displacements, which are unrestricted; thus, the system can accumulate large strains typical of natural, brittle materials. The numerical code that we use is RICEBAL, developed at Rice University, based on the open-source code TRUBAL [*Cundall and Strack*, 1979].

One of the appeals of the DEM approach is that very simple particle interactions yield distinctive, emergent behaviors at the system scale. Thus, discontinuities and heterogeneities can form and evolve in response to changing stress conditions and material properties. Conceptually, the approach resembles a numerical sandbox but offers added value by allowing material properties and mechanical states to be monitored and evaluated throughout the simulation and to be correlated with deformation behavior and structure. We have used this method successfully to simulate both small-scale processes, including fault gouge formation, evolution and mechanics [*Morgan and Boettcher*, 1999; *Morgan*, 2004; *Guo and Morgan*, 2007, 2008], landslide processes [*Katz et al.*, 2014], and large-scale geodynamic processes, such as volcano growth and deformation [*Morgan and McGovern*, 2005a, 2005b; *McGovern and Morgan*, 2009] and contractional deformation [e.g., *Dean et al.*, 2013; *Zhang et al.*, 2013]. The focus here is on the mechanics of fold and thrust belt evolution under tectonic loading.

Our implementation of DEM in RICEBAL is summarized here. A general schematic for particle interactions is shown in Figure 1a. Figures 1b and 1c show the resulting force-displacement relationships and interparticle failure criteria, respectively.

3.1. Interparticle Contact Forces and Bonding

Particles within the assemblage are assigned elasto-frictional contacts, which define the force-displacement relationships (Figure 1b). When particles come into contact, resistive forces arise from the elastic response of the particles. Repulsive normal forces (f_n) on particle boundaries are calculated as:

$$f_n = k_n \delta_n, \quad (1a)$$

where k_n represents the normal interparticle stiffness and δ_n denotes the amount of overlap between particles [*Cundall and Strack*, 1979]. A positive value for overlap indicates that the particles are in contact. Shear forces resulting from particle interaction are calculated using a similar relationship:

$$f_s = k_s \delta_s, \quad (1b)$$

where k_s dictates the shear stiffness between the particles and δ_s is the shear offset of the particle centers. Although stated very simply here, both the k_s and k_n values are nonlinear quantities related to the contact area of overlapping particles, as well as the particle shear modulus, G_p , and Poisson's ratio, v_p , following the Hertz-Mindlin theory [*Johnson*, 1985; *Morgan and Boettcher*, 1999; *Morgan and McGovern*, 2005b]. The shear forces at interparticle contacts are also limited by friction on the particle surfaces (μ_p), as

$$f_s^{\max} = \mu_p f_n \quad (2)$$

in the absence of bonding (Figure 1c). When f_s^{\max} is reached, slip occurs, allowing particles to slide past each other. By this mechanism, discrete structures, e.g., faults, can develop and grow.

In the simulations presented here, interparticle bonding is used to impart cohesion to the material assemblage. The bonds are defined as elastic cylinders that connect the centers of the particles in bonded

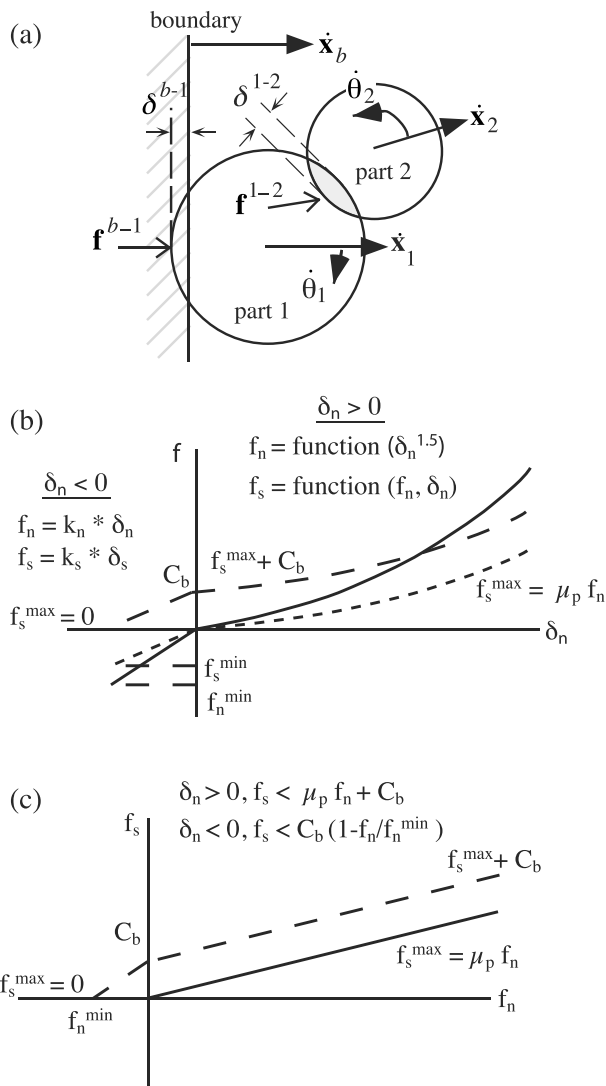


Figure 1. Implementation of DEM used here. (a) Schematic diagram of particle interactions. Lateral velocity of the boundary \dot{x}_b causes displacement and overlap with particle 1 of δ^{b-1} , imparting a force \mathbf{f}^{b-1} and acceleration of particle 1. The resolved velocity \dot{x}_1 and subsequent displacement of particle 1 cause overlap with particle 2 of δ^{1-2} , imparting a contact force \mathbf{f}^{1-2} with both normal and shear components. The resultant force causes both linear and angular accelerations on both particles, which are integrated to determine instantaneous velocities, $\dot{x}_1, \dot{x}_2, \dot{\theta}_1$, and $\dot{\theta}_2$. If the contact shear stress is high enough, sliding can also occur. (b) Force displacement relationships. Nonlinear (Hertzian) contact relationships operate under compression ($\delta_n > 0$), normal contact (solid line), noncohesive maximum shear force for $\mu = 0.5$ (short dashes), and cohesive maximum shear force (long dashes). Linear relationships apply to bonded particles in tension ($\delta_n < 0$). (c) Resulting interparticle failure criteria in both compression and tension, in terms of normal and shear forces, defining conditions leading to bond breakage (long dashed line) and interparticle sliding (solid line).

contact. As shown in Figure 1b, bond forces are zero when particles are not displaced relative to each other, i.e., $\delta_n = \delta_s = 0$. However, when particles are displaced in tension, the bonds can support tensile and shear forces below predefined tensile strength and unconfined shear strength (i.e., at $f_n = 0$). In interparticle compression, the shear forces that can be sustained are augmented by the assigned interparticle unconfined shear strength (Figure 1b). Relationships between interparticle shear and normal forces are shown in Figure 1c. By design, interparticle bonds in this implementation do not support moment and thus do not resist particle rotation. This allows for modest inelastic, nonbrittle deformation, consistent with the behavior of natural materials. Bond-induced interparticle forces are calculated as

$$f_n = E_b \delta_n * A \quad (3a)$$

$$f_s = G_b \delta_s * A \quad (3b)$$

where f_n and f_s are the tensile and shear force, respectively, and E_b and G_b are the Young's modulus and shear modulus of the bond, respectively. A_b is the cross-sectional area of the elastic bond, assumed to be a circle with a radius equal to that of the smallest particle in contact. Bond tensile forces are generated when particles are separated (i.e., $\delta_n < 0.0$) and are limited by the tensile strength, T_b , scaled by bond area, i.e., $T_b * A_b$. Bond shear forces can be supported in both tension and compression and are limited by

$$f_s^{\max} = C_b / T_b (T_b * A_b - f_n) \quad (4a)$$

$$f_s^{\max} = C_b * A_b + \mu_p f_n \quad (4b)$$

for $f_n < 0$ and $f_n > 0$, respectively, where C_b is the unconfined shear strength of the interparticle bonds at $f_n = 0$. Thus, the properties and strength of each bond are defined by the bond properties, specifically E_b , G_b , T_b , and C_b .

3.2. Particle Motions

For each time step, net force and moment are calculated for each particle by summing the components of all contact forces acting on a particle. These quantities are used to determine net linear and angular accelerations from which particle displacements and rotations are determined.

Table 1. Particle Properties for DEM Simulations^a

Unit	Radii (m)	Shear Modulus (Pa)	Poisson's Ratio	Friction Coefficient	Density (kg/m ³)
Upper plate	60,80	2.9E09	0.2	0.30	2500
Décollement	60,80	2.9E09	0.2	0.00	2500
Lower plate	60,80	2.9E09	0.2	0.30	2500

^aTime step: 0.05 s, wall displacement between increments: 160 m, and wall velocity: 2 m/s.

The net force (F_p) and net moment (M_p) are calculated by

$$F_p = m_p \ddot{x}_p \quad (5a)$$

$$M_p = I_p \ddot{\theta}_p \quad (5b)$$

where m_p and I_p are the mass and moment of inertia and \ddot{x}_p and $\ddot{\theta}_p$ are the linear and angular accelerations, respectively. Incremental particle displacements and rotations are calculated by inverting and twice integrating equations (5a) and (5b) over each time step, leading to new particle positions and orientations. The new particle configuration necessitates recalculating of contact forces, and the cycle is repeated. At each time step, particle motions are partially damped to dissipate energy in the system, a proxy for inelastic deformation in real materials. This damping approach is the one most commonly used [e.g., Cundall, 1987; Itasca Consulting Group, 1999], primarily due to its simplicity, although a variety of alternative approaches are available [Cundall, 1987; Walton, 1995].

3.3. Pore Pressures and Strength Evolution

Note that pore pressures are not simulated in these models but are treated implicitly through reduced strength zones such as the décollement. In this implementation, interparticle friction values do not change within the model throughout the simulation, precluding slip- or velocity-dependent changes in interparticle strength. Material strength throughout the rest of the domain, however, evolves naturally as bond breakage causes a loss of cohesion, and changes in particle packing induce compaction or dilation.

4. Stress Analyses and Material Calibration

The mechanical investigation of simulated contractional wedges requires determination of the bulk mechanical properties of the numerical materials, which are controlled by both particle properties and interparticle bond parameters [Potyondy and Cundall, 2004], as presented in Tables 1 and 2, respectively. In order to examine the effects of cohesion on wedge evolution, five different sets of bond parameters were used, defining distinct materials referred to as Types A (noncohesive), B, F, I, and Y. The letters correspond to parameter sets used for a subset of contractional simulations within a larger suite, only five of which are discussed here. Numerical calibration experiments were carried out to characterize the mechanical properties, prior to the analysis of the wedge simulations.

4.1. Calculating Stress

Although the DEM simulates discontinuous materials, equivalent continuum properties can be calculated throughout a domain by averaging micromechanical properties for particles [Oda and Iwashita, 1990]. In particular, the average two-dimensional stress tensor over a domain is calculated by summing the

Table 2. Interparticle Bond Properties for DEM Simulations

Model/Unit	Young's Modulus (Pa)	Shear Modulus (Pa)	Tensile Strength (Pa)	Cohesion (Pa)
A (upper)	-	-	-	-
B (upper)	2.0E08	2.0E08	1.0E7	2.0E7
F (upper)	2.0E08	2.0E08	2.0E7	4.0E7
I (upper)	2.0E08	2.0E08	3.0E7	6.0E7
Y (upper)	2.0E08	2.0E08	4.0E7	8.0E7
Décollement	-	-	-	-
Lower plate	2.0E08	2.0E08	4.0E7	8.0E7

normalized directional components of m contact forces acting on N particles [e.g., Cundall and Strack, 1983; Thornton and Barnes, 1986; Morgan, 1999; Morgan and McGovern, 2005b]:

$$\sigma_{ij} = \frac{1}{V} \sum_{p=1}^N \left[\sum_{a=1}^m \left(r_i^a f_j^a \right) \right]_p, \quad (6)$$

(in indicial notation; $i, j = 1, 2$), where σ_{ij} represent the components of the average two-dimensional stress tensor, V is the volume of the averaging domain, r_i^a are the components of the particle radius normal to the contact, and f_j^a are the total force acting in the j^{th} direction. The gridded directional components of the stress tensor then can be fit to continuous surfaces for plotting using Generic Mapping Tools [Wessel and Smith, 1995]. To obtain a relatively smooth approximation of continuum stresses within the discontinuous material, interparticle forces are averaged over 25–30 particles for each gridded stress tensor (elements are 500 m × 500 m).

Consistent with sediment and soil mechanics principles [e.g., Muir Wood, 1990], invariants of the two-dimensional stress tensor are used, in particular, the mean and differential stress, i.e.,

$$\sigma_m = \frac{\sigma_I + \sigma_{II}}{2}, \quad (7a)$$

$$\Delta\sigma = (\sigma_I - \sigma_{II}), \quad (7b)$$

respectively, defined in terms of maximum and minimum compressive stresses, σ_I and σ_{II} . Plotting $\tau_{\max} = \Delta\sigma/2$ simplifies the comparison to Mohr-Coulomb failure.

4.2. Biaxial Experiments

The bulk mechanical properties of the five different numerical materials used in these simulations, prescribed by particle properties and bond parameters in Tables 1 and 2, were obtained through two-dimensional biaxial compression and tension experiments. The bond parameters were selected to capture the general range of bulk material properties of soft sediments [Hoshino et al., 1972; Camac et al., 2009; Schumann et al., 2014] and the calibration tests carried out to constrain the resulting bulk properties. Material behavior depends on many particle-based properties, and few systematic investigations have been carried out to investigate their effects in numerical materials [e.g., Potyondy and Cundall, 2004; Schöpfer et al., 2007a, 2013]. This study therefore contributes to the overall characterization of such materials.

Test samples were constructed by generating ~1500 particles with the same properties and relative abundances as the contractional experiments, within an 8 km wide domain bounded by walls of fixed particles (Figure 2a). Two horizontal confining walls were constructed of rows of particles fixed to each other in a given wall. The walls were moved inward until the assigned vertical preconsolidation stress was reached. Preconsolidation stresses, P_c , of 2, 5, and 10 MPa were imposed, spanning the range of initial vertical stresses induced by gravitational loading within the ~6 km thick particle packing in the contractional experiments. Following preconsolidation, particles within the horizontal walls were unfixed relative to each other and assigned inward directed forces to define flexible “membranes” to constrain the sample and apply the confining stress.

Biaxial compression was induced by capturing particles within the vertical walls adjacent to the preconsolidated sample, defining lateral platens, and moving them inward at a constant rate of displacement until the sample failed along one or more inclined faults (Figures 2b and 2c). Failure was accommodated by interparticle bond breakage, both in tension and in shear. Confining stresses of 0.1, 10, 20, 30, 40, 50, 60, 70, and 80 MPa were applied and maintained by the membrane during biaxial compression. Biaxial tension was generated by moving the particles within the vertical walls outward at a constant rate until the sample fractured along a subvertical plane. Confining stresses were maintained at 0.1 MPa or less to ensure true tensile failure. Platen extenders constructed of additional fixed particles prevented membrane particles from escaping as the platens moved. Sample stresses were monitored throughout each test.

4.3. Mechanical Properties of the Numerical Materials

Each numerical biaxial compression test followed a consistent loading path, reaching a peak stress followed by a stress decrease to fluctuate around a lower value, approximating the residual strength [e.g., Jaeger and Cook, 1979]. Identical preconsolidated samples were deformed biaxially under different confining pressures;

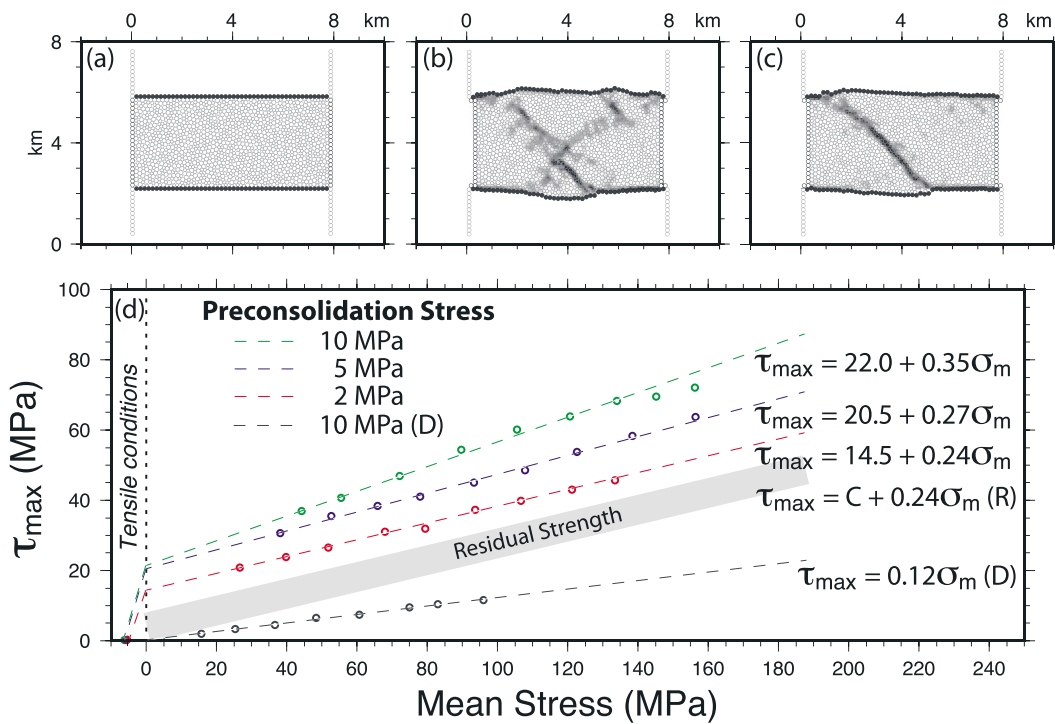


Figure 2. Setup and representative results of numerical calibration experiments. (a) Initial configuration of sample to be used for biaxial compression and tension experiments following consolidation to P_c of 10 MPa. Initial sample length is 8 km. (b) Sample shown in Figure 2a deformed in compression under confining stress of 2 MPa, following 5.5% axial strain. Distortional strain field shows the development of several localized shear bands. (c) Sample shown in Figure 2a deformed in compression under confining stress of 10 MPa, following 6% axial strain. Distortional strain field shows development of a single throughgoing shear band. (d) Peak strengths prior to brittle failure for material Type Y, preconsolidated to different values of P_c , and deformed under a range of confining pressures. Data are plotted in $\tau_{\max} - \sigma_m$ space. The slopes and intercepts of the best fit lines are used to calculate the Mohr-Coulomb failure line for the material. Tensile strengths are shown for each material as well. The derived mechanical properties for all materials are given in Table 3.

the resulting peak strengths define linear trends, when plotted in $\tau_{\max} - \sigma_m$ space. The slopes and intercepts of the best fit lines (e.g., Figure 2d) are used to calculate the Mohr-Coulomb failure line for the material, defined as

$$\tau^P = C_o + \tan(\phi)*\sigma_n, \quad (8)$$

where τ^P and σ_n are the peak shear stress and normal stress on a given plane at failure, ϕ is the slope of the failure line, and C_o is the material cohesion. The derived values for all materials used in these simulations are given in Table 3.

Derived cohesion values span a wide range, varying both with material bond strength and with P_c . For a given material (e.g., Types A, B, F, I, and Y), C_o increases with increasing P_c , except for the noncohesive materials (Type A), for which C_o is essentially zero. For a given value of P_c , C_o increases with increasing bond strength; i.e., it is lowest for unbonded Type A and highest for Type Y, reaching $C_o = 23.5$ MPa for the highest P_c . This value of cohesion is consistent with the strength of shallow crustal sediments [Jaeger and Cook, 1979; Camac et al., 2009], as well as sediments found in accretionary prisms [e.g., Schumann et al., 2014].

The values of ϕ also vary with material bond strength and with preconsolidation state. Across the highest bond strength series Y, ϕ ranges from $\sim 13^\circ$ for $P_c = 2$ MPa to $\sim 20^\circ$ for $P_c = 30$ MPa. The range of ϕ for the noncohesive material, Type A, is ~ 17 – 22° . Note that all of these values are significantly lower than the typical value of $\phi = 30^\circ$ [e.g., Jaeger and Cook, 1979], which is a common characteristic of these numerical materials [Morgan, 1999, 2004; Aharonov and Sparks, 2004; Dean et al., 2013], and consistent with shear experiments on smooth glass rods [Frye and Marone, 2002]. For materials at residual strength, ϕ appears to range around 12.5 – 14° , although with high uncertainty. The weakest material, Type D, defining the décollement, has ϕ of 6.9 – 7.5 and even lower residual value of 5.4° .

Table 3. Mechanical Properties Derived From Biaxial Compression and Tension Experiments

Material Suite	P_c (MPa)	Intercept (MPa)	Slope	C_0 (MPa)	Friction Coefficient	Friction Angle	T_0 (MPa)
A series	2.0	0.0	0.30	0.0	0.31	17.5	-
	5.0	0.0	0.32	0.0	0.34	18.7	-
	10.0	0.0	0.37	0.0	0.40	21.7	-
	30.0	0.0	0.37	0.0	0.40	21.7	-
B series	2.0	2.5	0.26	2.6	0.27	15.1	1.1
	5.0	5.0	0.29	5.2	0.30	16.9	1.8
	10.0	5.5	0.33	5.8	0.35	19.3	2.0
	30.0	5.5	0.34	5.9	0.36	19.9	2.0
F series	2.0	7.0	0.23	7.2	0.24	13.3	2.0
	5.0	9.5	0.29	9.9	0.30	16.9	3.1
	10.0	12.0	0.32	12.7	0.34	18.7	3.5
	30.0	12.5	0.32	13.2	0.34	18.7	3.2
I series	2.0	10.5	0.24	10.8	0.25	13.9	3.4
	5.0	16.5	0.26	17.1	0.27	15.1	4.1
	10.0	18.0	0.31	18.9	0.33	18.1	4.3
	30.0	18.0	0.32	19.0	0.34	18.7	4.3
Y series ^a	2.0	14.5	0.24	14.9	0.25	13.9	5.2
	5.0	20.5	0.27	21.3	0.28	15.7	6.1
	10.0	24.5	0.32	25.9	0.34	18.7	6.5
	30.0	22.0	0.35	23.5	0.37	20.5	7.0
Residual	-	<5.0	0.22–0.24	<5.0	0.23–0.25	12.5–14.0	-
Décollement series	2.0	0.0	0.13	0.0	0.13	7.5	-
	5.0	0.0	0.13	0.0	0.13	7.5	-
	10.0	0.0	0.12	0.0	0.12	6.9	-
	30.0	0.0	0.13	0.0	0.13	7.5	-
Décollement residual	-	0.0	0.09	0.0	0.09	5.4	-

^aMechanical properties also apply to underthrust plate.

Peak strength and subsequent strain weakening of tested samples were accompanied by the formation of distinct failure surfaces (Figures 2c and 2d). The orientation of these surfaces is a test of the reliability of the measured values ϕ , given the relationship between fault orientations and slope of the Coulomb failure criterion [e.g., Jaeger and Cook, 1979]. Several measured fracture surfaces are inclined 39–43° to σ_1 , which is higher than the typical inclination of 30° for most geologic materials, but consistent with the lower ϕ values of these numerical materials, as well as some idealized analog materials [e.g., Frye and Marone, 2002].

Biaxial tension tests resulted in extensional failure, defined by tensile strength T_0 . Values of T_0 are consistently 10% to 35% lower than C_0 and for a given material, generally increase with increasing P_c (Table 3). T_0 reaches 7.0 MPa for material Type Y at the highest P_c but only 2.0 MPa for material Type B. Again, this range of tensile strengths, although not activated under the stress conditions of these simulations, is consistent with the soft marine sediments noted above.

5. Design of Contractional Simulations

The contractional simulations presented here were initialized by randomly generating particles within a 120 km wide × 15 km tall domain. Particles were allowed to settle under gravity, bounded by two vertical walls and a basal row of fixed particles. The particle packing consisted of two particle sizes, with radii and abundances of 60 m and 80 m and 34,000 and 20,000, respectively. To examine the influence of bond strength and resulting material cohesion on wedge evolution, five simulations were carried out on initially identical homogeneous packings and boundary and initial conditions and dimensions (Table 1) but using different sets of interparticle bond parameters (Table 2). Upon settling, bonds of assigned strengths (Table 2) were introduced at all interparticle contacts, except along a 100 m thick décollement layer positioned ~950 m above the base of the domain. Interparticle friction was set to 0.3 throughout the bonded domain and to 0.0 within the décollement layer to ensure its lower strength (Table 1). From previous calculations, these interparticle friction values yield bulk sliding friction coefficients of about 0.3 and 0.1, respectively [Morgan, 2004], with little appreciable change with particle size [Morgan, 1999]. The new biaxial tests summarized above refine these values for the numerical materials used here. Interparticle friction along

the vertical walls was set to 0.0 to allow free slip during wedge growth. Colored layers within the bonded domains serve as strain markers during deformation but denote no contrast in mechanical properties.

Horizontal contraction was initiated by capturing particles along the left sidewall and applying a constant velocity to the right of 2.0 m/s. The lowest 950 m height of the wall stayed fixed, defining a "window" through which the underthrust (blue) sediments pass. The time step per cycle was 0.05 s, producing 0.1 m of wall displacement per cycle. Slip localized along the décollement, above the deepest 950 km blue layer, which defined a cohesive, elastic substrate, i.e., underthrust channel. To maintain the confining stress and prevent extrusion of this substrate following passage of the wall, new 40 m radius particles were created in the wake of the moving wall. The blue underthrust substrate was also rebonded every 16,000 cycles (1600 m wall displacement) to maintain its coherence.

Throughout the simulations, particle positions and interparticle forces were output every 1600 cycles (160 m wall displacement), an interval referred to as an "Increment." Subsequent calculations of particle displacements and mean particle stresses are made at whole increments, and this unit is used for plotting purposes.

6. Strain Analysis and Deformation Fields

6.1. Strain Analysis

Incremental and total particle displacements were derived for each new particle configuration (Increment) and resolved into horizontal and vertical components. A nearest-neighbor searching algorithm [Wessel and Smith, 1995] was used to grid the horizontal and vertical displacements at 120 m spacing, and a continuous surface was fit to each component. The directional derivatives of the two components yielded the four terms of the two-dimensional displacement gradient tensor; i.e., $D_{ij} = \partial u_i / \partial x_j$, (in indicial notation; $i, j = 1, 2$), where u_i are the components of the gridded displacement vectors.

Invariants of the finite strain tensor, \mathbf{E} , were derived to characterize the deformation field in time and space [e.g., Malvern, 1969]. The first invariant of the finite strain tensor, I_E , is a measure of volumetric strain and is derived from the deformation gradient tensor, \mathbf{F} , with terms $F_{ij} = \partial x_i / \partial X_j$, where x_i and X_j are the deformed and undeformed coordinates, respectively. The determinant of \mathbf{F} ,

$$\det(\mathbf{F}) = (\partial x_i / \partial X_j * \partial x_j / \partial X_i - \partial x_i / \partial X_j * \partial x_j / \partial X_i), \quad (9)$$

quantifies the ratio between deformed and undeformed volumes, v and V , respectively. Thus, I_E (volume strain) can be calculated as

$$I_E = v/V - 1.0 = \det(\mathbf{F}) - 1. \quad (10)$$

Strain-induced distortion can be quantified as the second invariant of the deviatoric finite strain tensor, II_E , where $\mathbf{E}' = \mathbf{E} - I_E/2$. II_E can be calculated in terms of the components of \mathbf{E} as

$$II_E = 0.5(E_{ij}E_{ij}) - 0.25(I_E)^2. \quad (11)$$

6.2. Distribution of Deformation

Comparative plots of the final particle configurations (Increment 200, i.e., 32 km wall displacement) of the five simulations are shown in Figure 3. Maps of the cumulative distortional strain and volumetric strain are shown in Figures 4 and 5, respectively. With increasing material cohesion, deformation becomes increasingly localized. The noncohesive Model A shows a smooth surface profile, and broad warping or folding of colored strata (Figure 3a), which is accommodated by largely distributed shear deformation with occasional local zones of more intense top-to-the-right shearing (Figure 4a, red zones). The intensity of shear deformation increases toward the moving wall (to the left). Experiments with higher cohesion (Models B, F, and I; Figures 3b–3d and 4b–4d) show progressive localization and intensification of discrete top-to-the-right shearing within the wedge, defining clear forethrusts (red), until the highest cohesion Model Y (Figures 3e and 4e), which shows uniformly spaced imbricate forethrusts (red) with relatively little distributed deformation between the faults. Back thrusts (blue) occur in all of the simulations but show

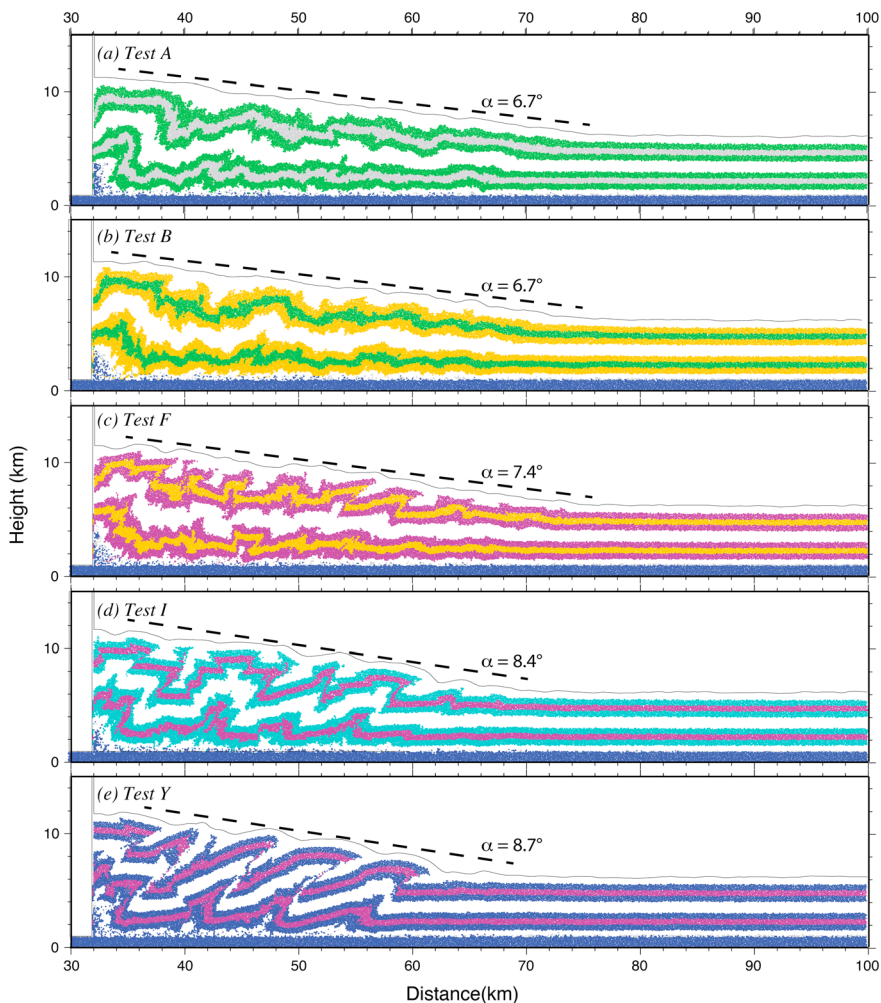


Figure 3. Final particle configurations for five contractual simulations, with increasing cohesion from top to bottom. Simulations extend to 120 km width, but images are cropped at 100 km for display. Colored layers serve as strain markers, revealing broad folds and fault offsets. (a) Model A–noncohesive system. (b) Model B–low cohesion. (c) Model F–modest cohesion. (d) Model I–high cohesion. (e) Model Y–highest cohesion.

relatively little displacement, and slip is predominantly along forethrusts. The length of the active basal décollement fault also increases with increasing material cohesion, tipping out just outboard of the deformation front (~ 85 km) on Model A but extending nearly to 100 km on Model Y. Another interesting trend evident on these plots is the tendency for back thrusts to form near the deformation front, before they become overwhelmed by displacement on the forethrusts.

As shown in Figure 5, all of the simulations also show cumulative tectonic volume loss, i.e., compaction (blue), caused by horizontal tectonic strain. Compaction is highest near the moving wall and decreases with distance but also is influenced by material cohesion. The lowest-cohesion experiments (Models A and B; Figures 5a and 5b) show broadly distributed compaction extending outboard of the deformation front and locally high dilation or contraction along zones of higher shear strain. This response reflects porosity loss due to the tighter packing of particles within the assemblage with increased horizontal strain. Higher-cohesion systems (Models I and Y; Figures 5d and 5e) show lower magnitudes of distributed compaction, but these zones now extend well outboard of the deformation front, nearly 100 km distance. The shallower strata show relatively little compaction and in fact sometimes exhibit distributed dilation. This effect is due to rotation of fault hanging walls, which decreases both horizontal and vertical loads acting on the block. In addition, the shallow reaches of the imbricate faults exhibit some local dilation, reflecting unpacking (dilation) of particles when localized shearing occurs.

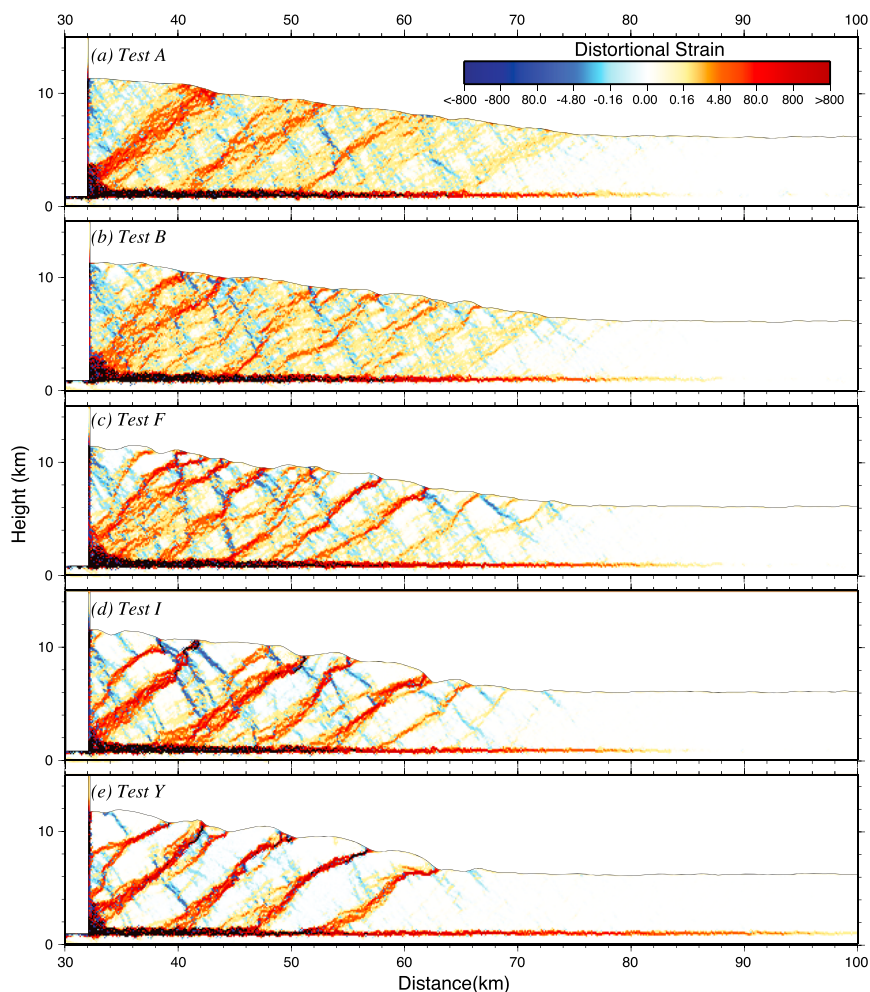


Figure 4. Final distortional strain field for five contractual simulations shown in Figure 2. Shear strain magnitude is shown by color intensity. Red denotes top to the right sense of shear; blue denotes top to the left sense of shear. (a) Model A–noncohesive system. (b) Model B–low cohesion. (c) Model F–modest cohesion. (d) Model I–high cohesion. (e) Model Y–highest cohesion.

7. Stress Analysis and Stress Evolution

7.1. Maximum Compressive Stress Distributions

The magnitude and orientation of the maximum compressive stress σ_1 is calculated and plotted for $1 \text{ km} \times 1 \text{ km}$ elements (summing over ~ 100 particles) to track stress magnitude and rotation. Comparative plots of the σ_1 vector fields for the end states of the five simulations show similar trends for all examples (Figure 6), broadly consistent with stress trajectories predicted for compressional systems from theory [Hafner, 1951; Mandl, 1988] and modeling [Souloumiac *et al.*, 2009]. Magnitudes of σ_1 increase downward and toward the moving left wall. Within the deformed wedge, σ_1 rotates with depth becoming inclined toward the décollement, due to frictional resistance to sliding. The noncohesive wedge, Model A (Figure 6a), shows a relatively smoothly varying σ_1 field, reflecting the relatively homogeneous material strengths across the domain. The higher-cohesion examples (Figures 6c–6e) show local variations in σ_1 , particularly in the vicinity of transiently active thrust faults and back thrusts, which deform under lower residual strengths. Rotation of σ_1 from subvertical (pretectonic) to inclined occurs outboard of the wedge tip in all examples, denoting the onset of significant slip along the décollement. The point at which σ_1 reorients is closest to the deformation front for the noncohesive wedge, Model A, occurring at ~ 90 km (Figure 6a), and most distant for the high-cohesion wedge, Model Y, exceeding the ~ 100 km cutoff of the plot (Figure 6e). The σ_1 vectors remain subvertical beneath the décollement, where vertical consolidation is the dominant history.

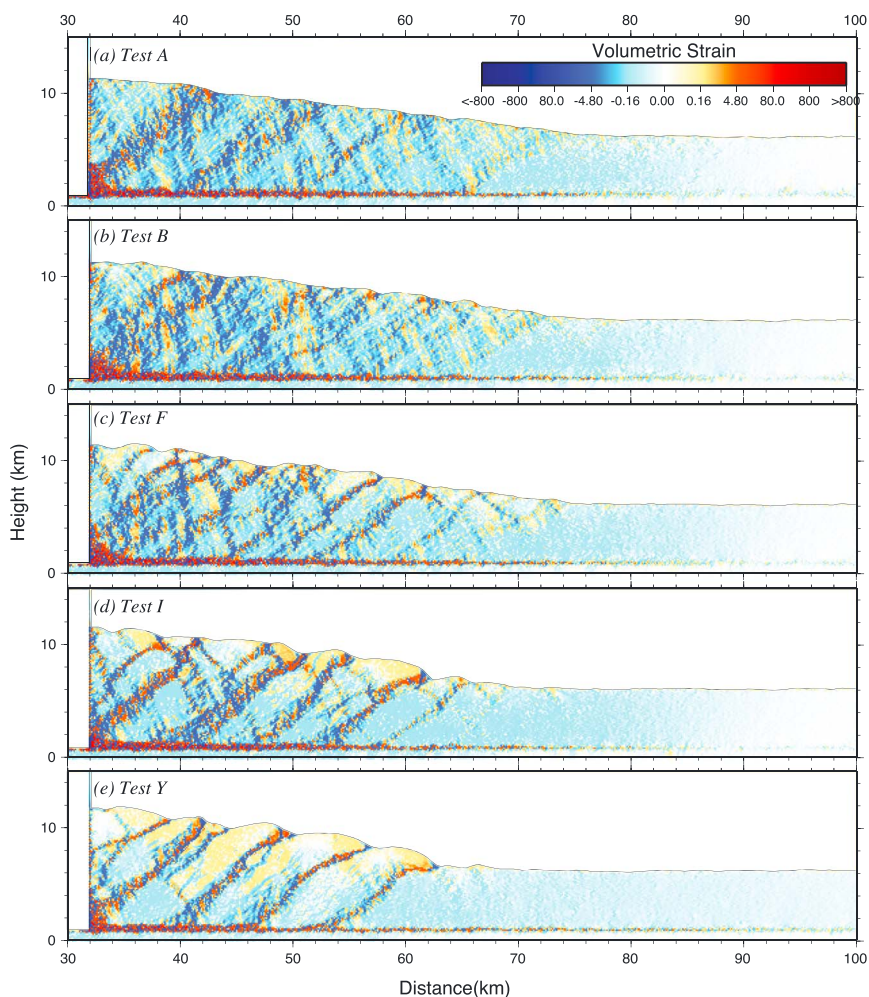


Figure 5. Final volumetric strain field for five contractional simulations shown in Figure 2. Volumetric strain magnitude is shown by color intensity. Blue denotes contraction and is broadly distributed throughout the model; red denotes dilation and tends to be concentrated within fault zones and in the hanging walls of thrust faults. (a) Model A–noncohesive system. (b) Model B–low cohesion. (c) Model F–modest cohesion. (d) Model I–high cohesion. (e) Model Y–highest cohesion. Derived values of cohesion for each material are given in Table 3.

7.2. Stress Invariants

The derived mean stress and maximum shear stress fields for the final states of the five simulations also vary with material strength and cohesion. Stress invariants for all of the systems are calculated and plotted for $1 \times 1 \text{ km}$ elements (summing over ~ 25 particles), with color scaled by stress magnitude. The final structure of each series (e.g., Figure 4) is superimposed by plotting regions of high distortional strain in black.

Mean stress, σ_m , generally increases with depth, and with proximity to the moving wall in all examples (Figure 7), reflecting the combined effects of higher vertical and horizontal loads. Maximum shear stress, τ_{\max} , shows greater variability within the wedges (Figure 8); τ_{\max} increases with depth due to the combined increase in both vertical and horizontal stresses with burial. Also, τ_{\max} is relatively high close to the moving wall and in the footwalls of major shear zones, which impart horizontal loading. The highest values of τ_{\max} are typically observed immediately in front of the frontal thrusts, outlining regions of unfaulted material that still supports high shear stresses. The frontal regions of high τ_{\max} expand with increasing material cohesion (Figure 8), demonstrating the enhanced ability of more cohesive materials to transmit high shear stresses. These regions also correspond to zones of high σ_1 magnitudes (Figure 6). Inclined bands of low τ_{\max} (in white) lie outboard of the high τ_{\max} zones in front of the deformed wedge (Figure 8). These τ_{\max} minima correspond to regions where the laterally increasing horizontal stress is similar to the vertical

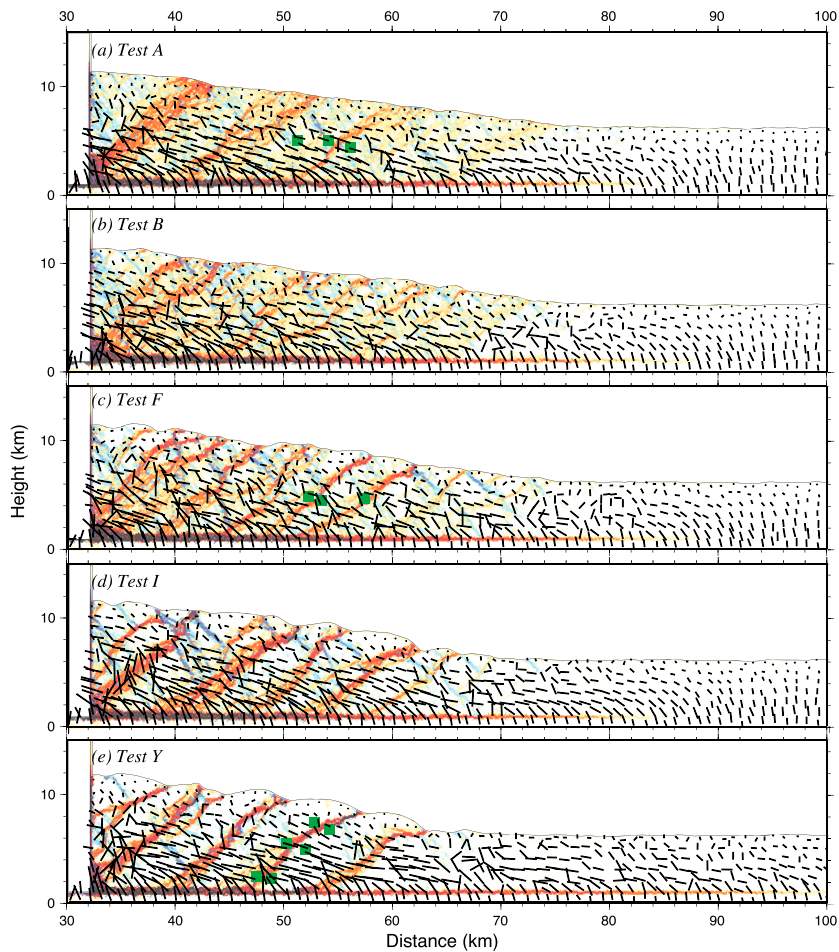


Figure 6. Final σ_1 fields for five contractional simulations shown in Figure 2, superimposed on distortional strain field from Figure 3; vector lengths scale with magnitude of σ_1 . (a) Model A—noncohesive system. (b) Model B—low cohesion. (c) Model F—modest cohesion. (d) Model I—high cohesion. (e) Model Y—highest cohesion. Derived values of cohesion for each material are given in Table 3. The green boxes show the final locations of elements tracked for stress paths in Figures 11 and 12.

consolidation stress; i.e., the stress state is nearly isotropic. These regions also coincide with the systematic rotation of σ_1 vectors from horizontal to vertical (Figure 6).

7.3. Failure Potential

The derived failure criteria for the model materials (Table 3), defined by their slopes and intercepts in $\sigma_m - \tau_{\max}$ space, can be used to predict material proximity to brittle failure within each system, referred to here as “failure potential.” More than one failure criterion applies for each simulation, due to the different initial preconsolidation stresses with depth prior to the onset of tectonic deformation (Table 3). Here the ratio of τ_{\max} to σ_m is compared to the strength criterion derived for P_c of 10 MPa, representative of the base of the undeformed strata.

Figure 9 shows the failure potential fields for the final configurations of the five simulations discussed above. In the noncohesive system, Model A (Figure 9a), failure potential is relatively high throughout the deforming wedge but decreases outboard of the wedge toe. The entire noncohesive wedge is essentially close to a state of failure, consistent with the predictions of critical Coulomb wedge theory [Davis et al., 1983]. In the more cohesive systems, the failure potential is typically highest near the deformation front of the wedges and in particular, in the footwalls of the frontal thrusts. These regions are most likely to fail next through the formation of a new forethrust or back thrust. The high failure potential regions thicken and lengthen with increasing material cohesion (Figures 9b–9f), corresponding with the increased reach of the active décollement (Figure 4) and reflecting the increasing ability of strong materials to transmit tectonic stress.

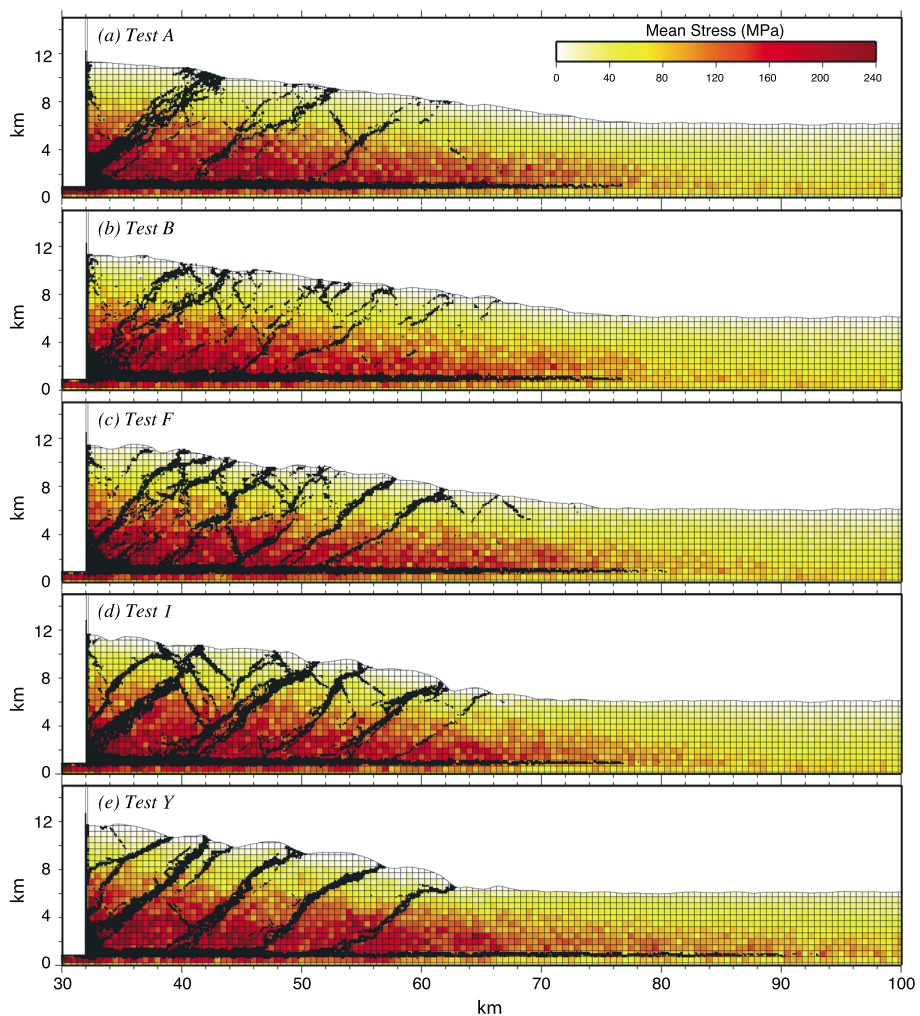


Figure 7. Final σ_m fields for five contractional simulations shown in Figure 2; stress intensity scales with color. (a) Model A—noncohesive system. (b) Model B—low cohesion. (c) Model F—modest cohesion. (d) Model I—high cohesion. (e) Model Y—highest cohesion. Derived values of cohesion for each material are given in Table 3.

The deformed wedges, in contrast, are characterized by lower values of failure potential. Here preexisting faults are slipping at their residual strengths, controlled by interparticle friction rather than cohesion. Local regions of moderate failure potential do occur within the deforming wedge, but these tend to lie between low-strength faults that accommodate sliding, keeping the interfault stress state below failure.

7.4. Thrust Initiation and Propagation

A closer look at the correlation between mechanics and kinematics is obtained by examining the formation of a discrete thrust fault in the most cohesive simulation, Model Y. Images from five sequential increments are shown (Figure 10), spanning wall displacements of 18.4 km (Increment 115) to 19.2 km (Increment 120). Three panels are plotted for each Increment, showing failure potential, incremental volume strain, and incremental distortional strain. Note that, in contrast to Figure 9, failure potential is calculated for elements gridded at 250 m \times 250 m, so as to resolve detailed features. The plots show incremental strains calculated for displacements accumulated between consecutive Increments. Again, regions of high cumulative distortional strain are superimposed in black to resolve the fault structure. Regions of incremental loading and unloading are outlined in solid and dashed lines, respectively, and labeled.

Increment 115 (Figure 10a) captures the end of active slip on two preexisting fault planes, T_2 and T_3 , and local slip on the décollement. The incremental volume strain plots (Figure 10a, middle) show a diffuse blue color across the domain, indicating overall volume loss, largely accommodated by recoverable elastic strain. High

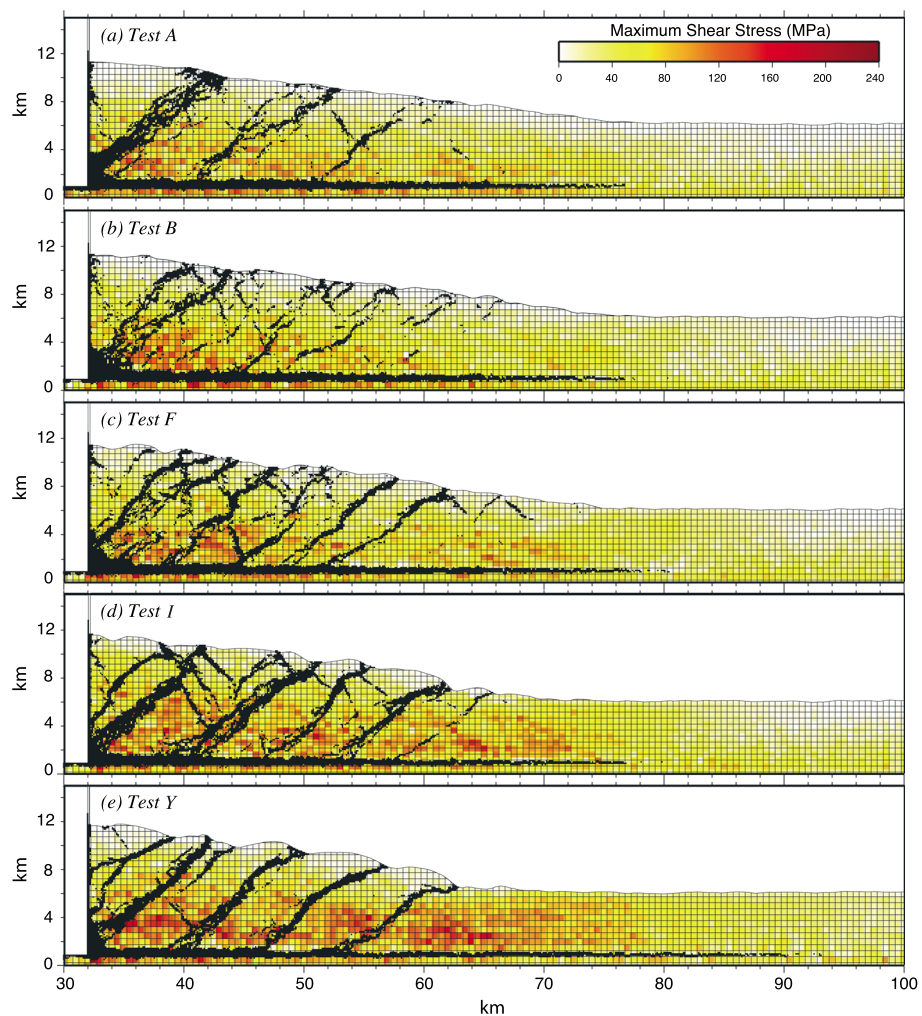


Figure 8. Final τ_{\max} fields for five contractional simulations shown in Figure 2; stress intensity scales with color. (a) Model A—noncohesive system. (b) Model B—low cohesion. (c) Model F—modest cohesion. (d) Model I—high cohesion. (e) Model Y—highest cohesion. Derived values of cohesion for each material are given in Table 3.

failure potential (Figure 10a, left) is evident in the footwall of the frontal thrust and locally at depth within the deforming wedge. A zone of high failure potential also spans the décollement at ~ 48 km (region 1), denoting local décollement locking. Tensile conditions (blue) are evident at the crest of the fold above the frontal thrust.

By Increment 117 (Figure 10b), the locked décollement has slipped, releasing region 1 and activating the décollement out to ~ 70 km or beyond (Figure 10b, right). A complex region of locking develops at 50–54 km distance (region 2). The décollement slip event also relieves the high failure potential within the deformed wedge while increasing the failure potential in the footwall of the frontal thrust (Figure 10b, left). Incremental volume loss (blue in middle plot) reflects further buildup of elastic contraction in the footwall. Decollement slip continues in Increment 118 (Figure 10c), failure potential increases further in the footwall (region 3), and a new region of décollement locking forms at 62–64 km (region 4).

Increment 119 (Figure 10d) exhibits a sudden change in state, with the initiation of a new thrust fault at a distance of ~ 45 km, where high failure potential was previously noted (region 3). This fault initially ruptures the shallowest strata (region 3a), where the failure potential was highest, causing a sudden decrease in failure potential near the surface (Figure 10d, left). Slip on the new fault also causes volume increase in the new fault zone, as well as both the hanging wall and footwall (red and yellow, middle plot), reflecting dilation during faulting, corresponding to elastic rebound of the wall rocks upon failure. This rupture, however, causes an increase in loading and failure potential at depth (region 3b). With continuing strain,

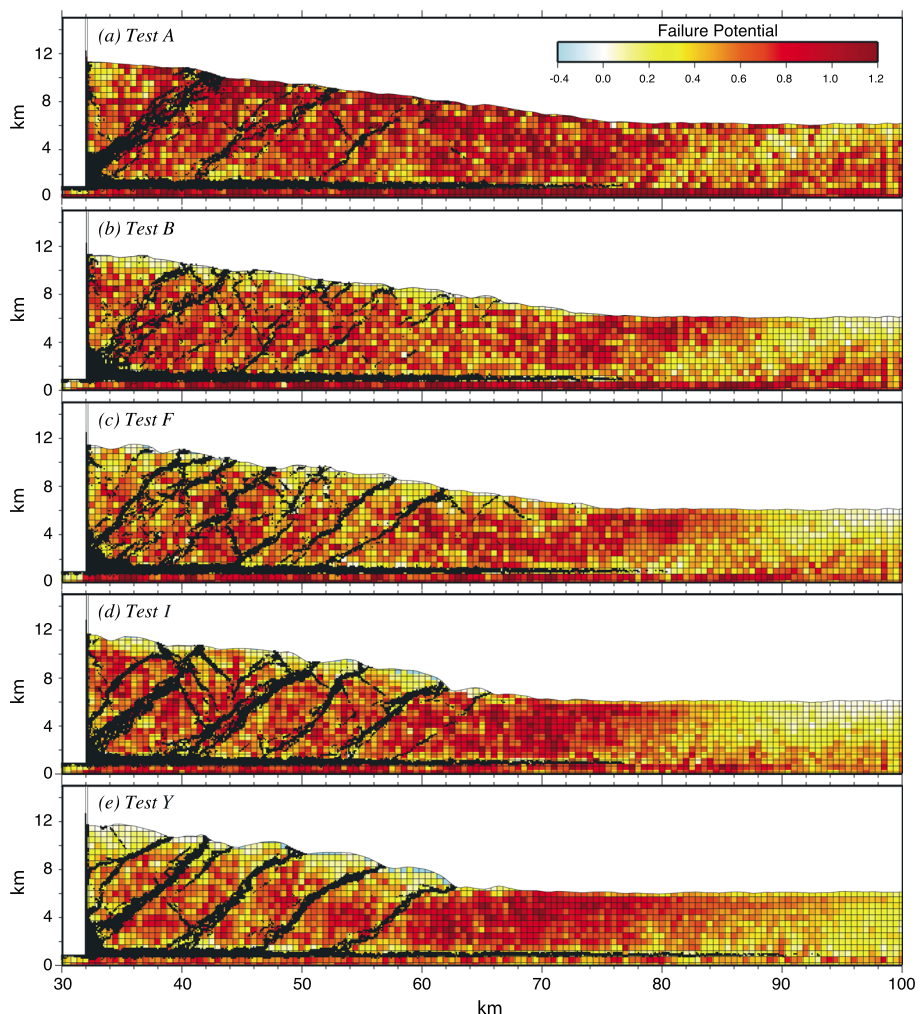


Figure 9. Final failure potential fields for five contractional simulations shown in Figure 2; failure potential scales with color. (a) Model A—noncohesive system. (b) Model B—low cohesion. (c) Model F—modest cohesion. (d) Model I—high cohesion. (e) Model Y—highest cohesion. Derived values of cohesion for each material are given in Table 3.

to Increment 120 (Figure 10e), the newly formed fault propagates downward through the high failure potential region 3b to the décollement (Figure 10e, right), relieving the failure potential across the area (region 3). Continued fault slip is accompanied by additional dilation and elastic rebound adjacent to the fault (Figure 10e, middle). By Increment 120, the high stresses spanning the décollement in regions 2 and 4 have been released, allowing renewed décollement slip out to ~70 km.

7.5. Stress Paths

Plots of stress quantities (Figures 6–9) indicate that cohesive strength influences the extent to which stresses are transmitted across a domain. A further demonstration of this lies in the stress evolution of specific elements throughout the simulations, as the deformation front approaches and passes by. Here elements correspond to small domains (1×1 km) composed of 65–85 particles, centered on a single particle that is tracked throughout the simulation, in contrast to the spatially fixed elements plotted in Figures 7–9. Values of τ_{\max} are plotted against Increments and back wall displacement for elements in three representative simulations in Figures 11 and 12, and compared to episodes of décollement propagation outboard of the most recent frontal thrust, and thrust fault activity where possible. All elements were initially located between 40 and 50 km distance from the back wall and are labeled according to their x positions at the start of the simulations. The final x positions are plotted at Increment 200 in Figure 6, showing their proximity to deformation structures that might influence their stress evolution.

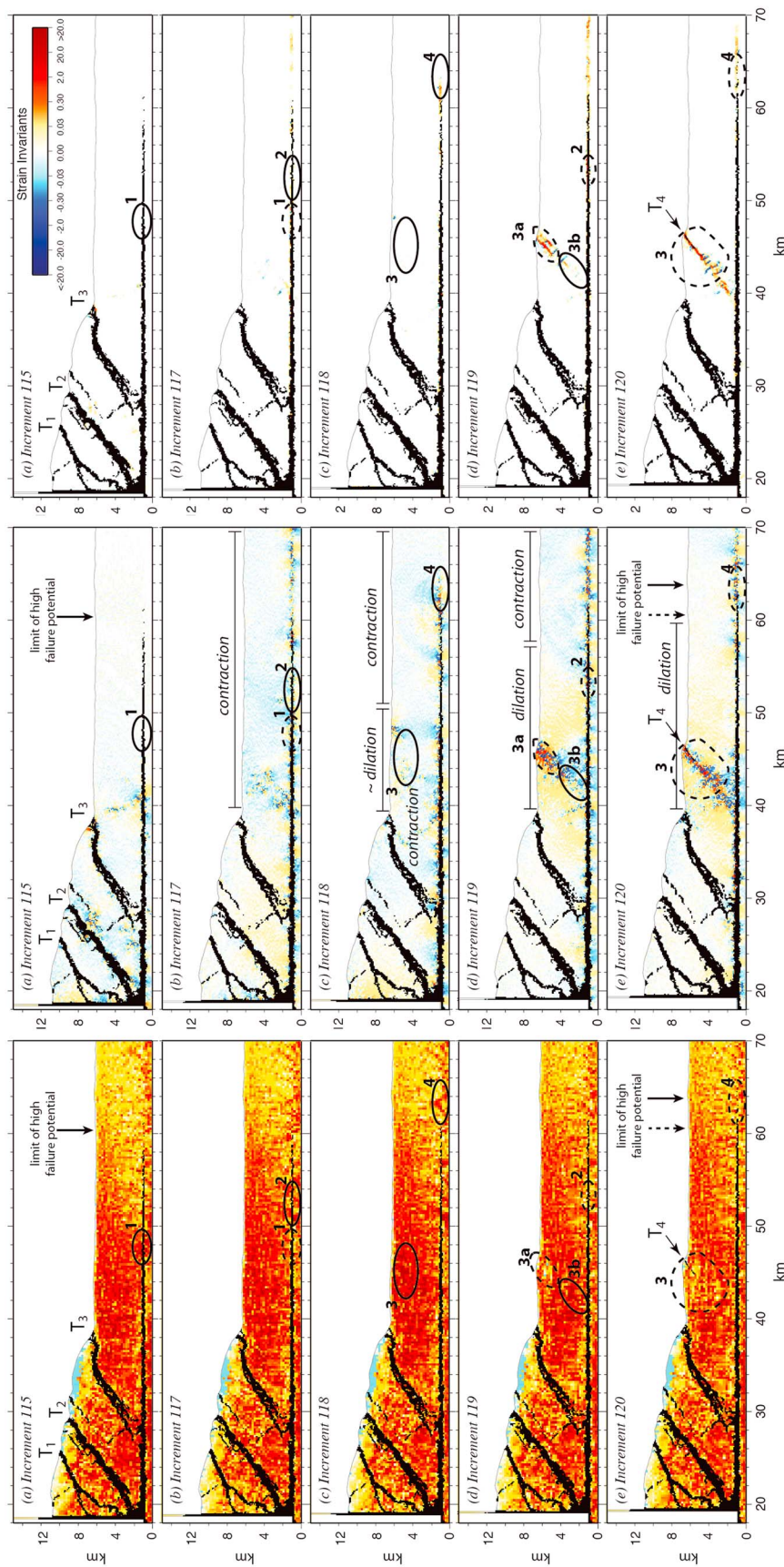


Figure 10. Correlated sequences of failure potential and incremental strain invariants during initiation of frontal thrust F_4 in Model Y, spanning wall displacement of 18.4 km (Increment 115) to 19.2 km (Increment 120). (left) Failure potential fields, colors as in Figure 9; (middle) incremental distortion strain; and (right) strain intensities map to the same colors shown in the upper right. (a) Increment 115–residual slip occurs on older faults, failure potential is high in shallow footwall of F_3 , and the décollement is locked at region 1. (b) Increment 117–décollement slip breaks through region 1 and locks at region 2, expanding the high failure potential. (c) Increment 118–initial rupture of F_4 breaks shallow frontal region, failure potential continues to increase in frontal region, with further slip on décollement, leading to locking at region 4. Contraction dominates. (d) Increment 119–failure potential propagates downward to the décollement, relieving high failure potential throughout the wedge; dilation accompanies rupture. (e) Increment 120–rupture propagates throughout the wedge; dilation dominates.

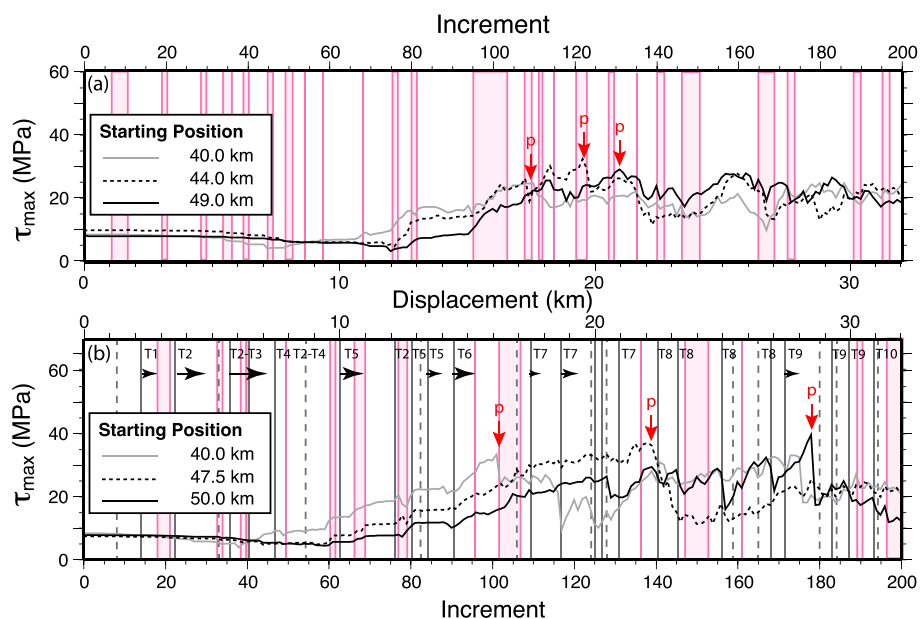


Figure 11. Stress paths showing τ_{\max} for elements initially located 3500 m above the model base from two simulations, tracked through the development of the contractional wedges. Final element locations are shown in Figure 6. (a) Three elements from Model A. (b) Three elements from Model F. Episodes of décollement propagation are shown by pink bands. Episodes of fault slip are shown as black lines (forethrusts) and dashed lines (back thrusts); the arrows denote enduring slip events. The red arrows labeled “p” denote peak values of τ_{\max} for a given stress path.

For Models A and F, three elements originally located ~3500 m above the model base are tracked (Figure 11). All elements start at τ_{\max} of ~9–10 MPa, and initially show slight declines with back wall displacement, as horizontal stress increases with little change in vertical stress. As décollement slip propagates outward, the elements begin to feel the onset of tectonic loading; τ_{\max} increases for each element in order of its position, as horizontal loading migrates outward. In Model A, this transition in loading occurs at Increment 60 for element 40.0 first at Increment 60, whereas for F, it occurs at Increment 40 for element 40.0. The loading stress paths tend to show stepped profiles, with distinct rises in τ_{\max} during episodes of décollement propagation (pink bars), and more stable τ_{\max} during the intervening periods, which generally correspond to internal shearing or thrusting.

The peak values of τ_{\max} are reached at different points for each element and simulation (Figure 11). For Model A, τ_{\max} reaches 25–30 MPa for all elements between Increments 105 and 130. In Model F, peak τ_{\max} values are closer to 35–40 MPa, but occur over a wider range of displacement, at Increment 102 for element 40.0, Increment 138 for element 47.5, and finally at Increment 178 for element 50.0. The peak stresses are distinctly correlated with deformation events, primarily décollement slip in Model A (Figure 11a), noting the relatively smooth passage of the deformation front in this unconsolidated system, but for Model F, stress drops correspond to both décollement slip (element 40.0) and fault slip (element 50.0). Despite the correlations with fault slip, however, the peak values of τ_{\max} do not necessarily correspond to failure. Beyond the plotted peak stresses, τ_{\max} values for all elements fluctuate around mean values closer to 20–25 MPa (Figure 11). This lower range of τ_{\max} is consistent with a decline to residual strength, as noted in Table 3. The variations in τ_{\max} in these postpeak phases are somewhat difficult to parse out, although they also show direct correspondence to deformation events, variously showing loading and unloading behaviors, demonstrating a highly complex correspondence to heterogeneous wedge deformation.

7.6. Stress Paths Along a Thrust Fault

A clearer demonstration of the connection between stress evolution and deformation is obtained by tracking stresses within pairs of elements from the most cohesive Model Y located on either side of the fault T_4 examined in Figure 10. Element pairs are selected from three initial vertical positions: 2000 m (i.e., ~1000 m above the basal décollement), 3500 m, and 5000 (~1200 m below the top surface). Figure 12 shows the

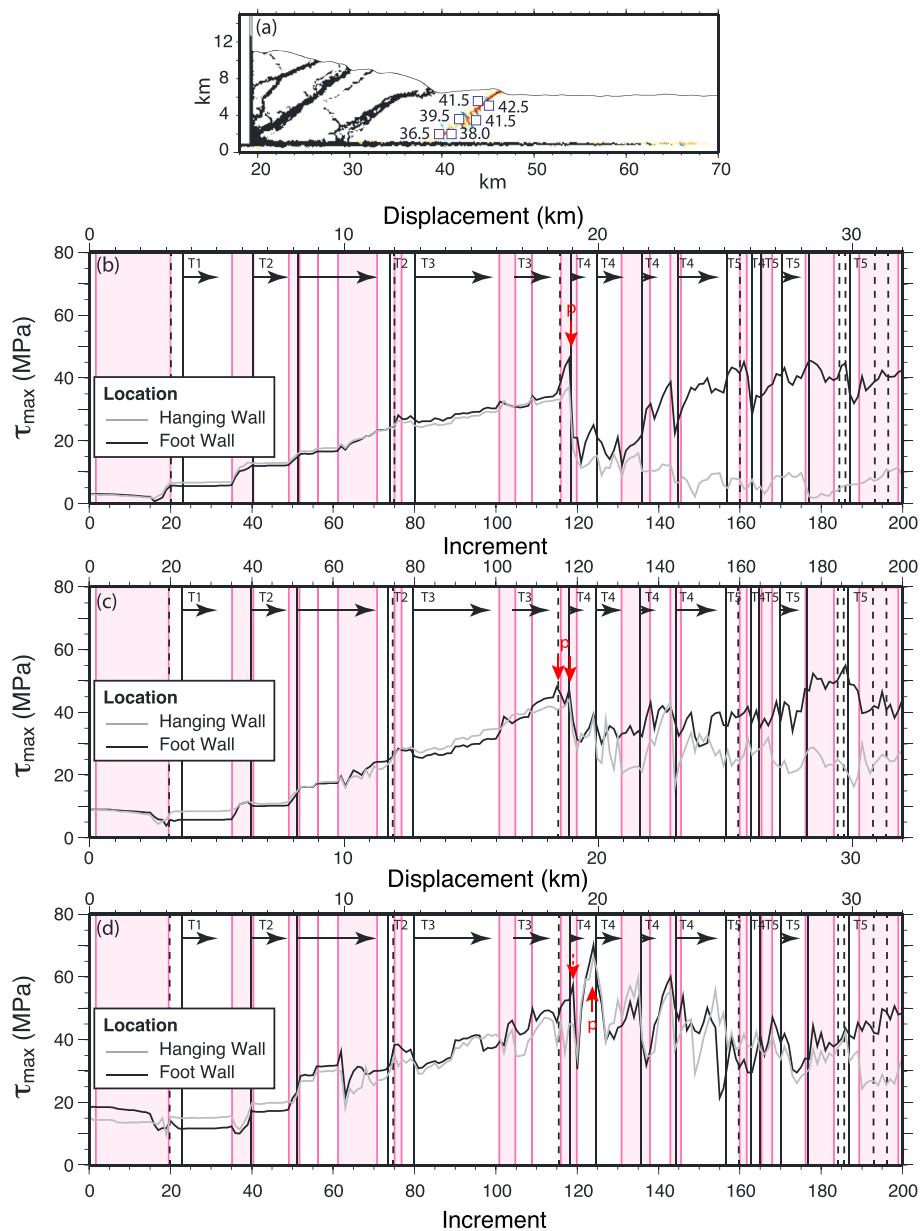


Figure 12. Stress paths showing τ_{\max} during Model Y for pairs of elements on either side of fault T₄, tracked through the development of the wedge. (a) Locations of elements immediately following formation of fault T₄; numbers correspond to initial x positions of elements. Final element locations are shown in Figure 6. (b) Element pair from 5000 m above model base. (c) Element pair from 3500 m above model base. (d) Element pair from 2000 m above model base. Episodes of décollement propagation are shown by pink bands. Episodes of fault slip are shown as black lines (forethrusts) and dashed lines (back thrusts); the arrows denote enduring slip events. The red arrows labeled p denote peak values of τ_{\max} for a given stress path.

locations of tracked elements at Increment 120 and τ_{\max} plotted against back wall displacement to examine the contrasting evolution of the two blocks.

The shallowest elements, originally positioned at 5000 m (Figure 12b), start at τ_{\max} of ~3 MPa and show very slight decreases in τ_{\max} during the initial stages of back wall displacement (Increments 1–15). By Increment 20, this phase gives way to step increases in τ_{\max} associated with episodes of décollement slip, until τ_{\max} reaches 38–48 MPa. When T₄ starts to form (Increments 119–120), both elements exhibit sudden decreases in τ_{\max} to ~12 MPa. During the initial phases of slip on T₄ (Increments 120–136), τ_{\max} fluctuates in tandem for both elements around relatively low values (~20 MPa). Beyond this point, the τ_{\max} paths for the

hanging wall and footwall elements diverge; the footwall element continues to fluctuate around relatively low τ_{\max} , whereas the hanging wall element rises again to τ_{\max} of ~50 MPa. To first order, the differences in mean values for the two elements are explained by the progressive loading of the footwall element during displacement along T_4 , whereas the hanging wall element experiences little change in mean stress during slip. Postrupture, both elements exhibit steps and drops in τ_{\max} that generally correlate with fault activity and décollement slip. These steps typically trend in the opposite directions; i.e., loading in the footwall coincides with unloading in the hanging wall (e.g., Increments 144 and 176) and vice versa (Increment 170).

The two elements originally at 3500 m (Figure 12c) start at τ_{\max} of ~9 MPa and show similar progressive loading trends with each other and with the shallower elements. Stepped increases in τ_{\max} again starting at about Increment 20, and continue until the initiation of T_4 (Increments 119–120), reaching 45–50 MPa prior to their sudden drop. At this point, the two paths diverge from each other. The footwall element ultimately climbs again to a τ_{\max} of ~55 MPa, whereas the hanging wall element fluctuates closer to ~30 MPa. The variations in τ_{\max} are generally positively correlated up to Increment 150, at which point a subtle negative correlation is evident, in particular during décollement slip events (e.g., Increments 168 and 189).

The deepest two elements, originally positioned at 2000 m (Figure 12d), start with τ_{\max} of 15–20 MPa, and again show the early onset of stepped stress paths prior to the formation of T_4 , rising to τ_{\max} of ~60 MPa at the point of fault rupture (Increment 120). In contrast to the shallower elements, however, distinct drops in τ_{\max} occur during the initial loading paths. This behavior reflects greater sensitivity to décollement activity, which contributes to stress buildup and release near the base of the wedge. A sudden drop in τ_{\max} to ~30 MPa upon the formation of T_4 is immediately followed by a rapid rise to 70 MPa, indicating further loading downdip of the propagating fault. A second episode of T_4 activity, starting at Increment 124, relieves this stress for both elements. From this point on, the stress paths of the two elements remain closely correlated, despite lying on opposite sides of the active fault. The stress paths only deviate significantly at Increment 189, where they exhibit a slight negative correlation. By the end of the simulation (Increment 200), the footwall element rises back to τ_{\max} of ~50 MPa, whereas the hanging wall element settles out τ_{\max} of ~30 MPa.

8. Discussion

8.1. Deformation Processes

The contractional simulations presented here, driven by translation of a rigid back wall into homogeneous particle packings, produced characteristic fold and thrust fault systems with typical wedge geometries [e.g., Davis *et al.*, 1983; Mulugeta, 1988]. Discrete faults, both forethrusts and back thrusts, developed in nearly all simulations but with varying degrees of localization and associated fault spacing (Figure 4). The lowest-cohesion Model A exhibits broad shear zones and folds rather than faults. These geometries occur in other particle-based simulations of noncohesive contractional wedges [e.g., Burbridge and Braun, 2002; Vietor, 2003; Naylor *et al.*, 2005], but are unlike typical sandbox models, which always exhibit discrete faults [e.g., Mulugeta, 1988; Koyi, 1995; Yamada *et al.*, 2006]. This discrepancy results from the mathematical perfection of the rounded particles, which can roll unimpeded [Morgan, 2004], resulting in low bulk strength relative to natural granular materials [e.g., Frye and Marone, 2002]. Rougher irregular sand grains exhibit more dilatant frictional sliding, resulting in localized faulting and higher frictional strength [e.g., Mair *et al.*, 2002]. To achieve the discrete faulting behaviors in the numerical simulations, consistent with natural Coulomb materials, interparticle bonding was introduced to impart modest bulk cohesion (Figure 2).

For the basal décollement strength and internal friction values used here, there is a clear preference for forethrusts to accommodate shortening and thickening of the wedge, although complementary conjugate back thrusts do develop, distributing deformation throughout the wedge. Back thrusting is observed in physical sandbox models as well, typically under low basal strength conditions [e.g., Cotton and Koyi, 2000; Cubas *et al.*, 2010], but also as more subtle, transient features in the frontal regions of the wedges as seen here [e.g., Ruh *et al.*, 2012]. An interesting feature observed in all of these simulations is the early generation of small offset back thrusts near the deformation front, typically before new forethrusts develop and

accommodate most of the horizontal shortening. This may be a manifestation of the minimum work principle [Del Castello and Cooke, 2007; Cooke and Madden, 2014], which predicts the vergence of new faults. This sequence of thrusting, influenced by the mechanical constraints discussed below, may be common in natural systems as well, although challenging to interpret based on field observations [e.g., Ruh *et al.*, 2012].

Interestingly, nearly all thrust faults initiate at shallow depths and propagate down toward the décollement over several time steps (e.g., Figure 10). This can be explained by the lower preconsolidation stresses of shallow sediments, resulting in lower bulk cohesive strengths, favoring early failure. Similar patterns have been observed in other particle-based models [Hardy *et al.*, 2009], and simulations based on minimum work reveal this tendency as well [Del Castello and Cooke, 2007]. This behavior, however, may not be fully representative of natural systems in which cohesion varies with depth.

An important characteristic of these particle-based simulations is the occurrence of substantial tectonic compaction, i.e., volume strain, prior to the onset of thrust faulting. This compaction influences the dynamics of the system, as the lateral consolidation, reduction in pore space, and increase in interparticle contacts enhance horizontal force transmission through the medium. The result is higher horizontal stresses, and eventually, higher differential and mean stresses, bringing the system closer to failure. The precursory change in material properties and stress state preconditions the system for brittle failure by thrusting, due to the need to overcome the enhanced compaction to accommodate further shortening. The dilative nature of newly formed faults is apparent in all of the simulations (e.g., Figure 5). The most dilative part of the system is at shallow depths where mean stresses are low, accounting for the tendency for faults to initiate in the upper section and propagate down over time.

Volumetric tectonic strain has been documented or inferred previously in various contractional systems. Significant horizontal shortening is accommodated by volume strain in sandbox models [e.g., Adam *et al.*, 2005; Nilforoushan *et al.*, 2008; Koyi *et al.*, 2004]. Porosity loss in marine sediments during accretion and tectonic shortening has also been documented and quantified [Bray and Karig, 1986; Morgan *et al.*, 1994]. Volumetric tectonic shortening can also occur by noncompactive means, e.g., through pressure solution in carbonates or other lithologies [Ferrill and Dunne, 1989; Onasch, 1994]. As a whole, such observations highlight the importance of including volumetric deformation in kinematic and continuum numerical models, in order to correctly predict the system behavior [e.g., Gray *et al.*, 2014].

The basal décollement plays a significant role in the behavior of the modeled systems. Designed as a weak horizon, slip is localized preferentially along the décollement. The partitioning of horizontal shortening above and below the décollement by differential displacements of the back wall causes decoupling of shear stresses across the fault (Figure 6). This decoupling, however, is incomplete; the décollement also exhibits spatial and temporal heterogeneities in strength and slip, controlled primarily by fault roughness in this particulate system. This is manifest as episodes of fault locking and release, as previously shown in particle-based models [e.g., Fournier and Morgan, 2012], and analogous to the seismic cycle along a convergent megathrust [Scholz, 1990]. Decollement locking causes the buildup of horizontal stresses in the overriding plate (e.g., Figure 10), enabling the formation of new thrust faults above the locked region. Unlocking causes rapid forward propagation of décollement slip, accompanied by the rapid release of elastic strains within the upper plate. Thus, the deformation front migrates forward episodically, accompanied by renewed tectonic compaction and stress rotation. The zone of tectonic compaction is generally limited to the region above the slipped décollement (Figure 5), defining the region that is preconditioned to undergo imminent brittle faulting.

8.2. Mechanical Conditions

Commonly, the gross wedge geometries of the contractional wedges are assumed to be described by critical Coulomb wedge theory [Davis *et al.*, 1983; Dahlen, 1990], providing a prediction for the final geometries of the simulated wedges. In the absence of pore fluid pressures, the main parameters controlling the force balance within a wedge are basal and internal friction coefficients. Cohesion is thought to play a secondary role, strengthening the wedge relative to the frictional strength, in particular near its thin toe, predicting a concave or convex up wedge taper [Dahlen *et al.*, 1984; Zhao *et al.*, 1986; Dahlen, 1990]. However, these predictions rely on the assumption that cohesion persists within a wedge that is on the verge of failure everywhere [Dahlen *et al.*, 1984]. Neither natural nor simulated materials behave this way; instead, fault formation results in strain weakening and localization, until the bulk mechanical strength is

controlled by the noncohesive residual strength of the wedge material [e.g., *Jaeger and Cook*, 1979; *Lohrmann et al.*, 2005]. Thus, a first-order prediction for the simulations, which have identical interparticle friction coefficients, is consistent surface slopes. In fact, mean surface slopes of all simulated wedges are similar by the end of the simulations, although slope angles increase slightly with cohesion (Figure 3), from 6.7° (noncohesive Model A) to 8.7° (Model Y). Thus, material cohesion appears to play a minor role in final wedge taper, but it may be overwhelmed by other factors discussed below.

A simple calculation of the predicted wedge tapers, after *Dahlen* [1984], demonstrates that the low basal and residual friction values for the model materials (Table 3) should yield even lower surface slopes than observed. A probable explanation for this mismatch is that the real basal friction angles in these systems are higher than 5.4–7.5° measured from biaxial experiments for the décollement materials (Table 3). The thinness of the décollement (~100 m) allows interactions between the higher-friction materials within the wedge and the underthrust package, evident from the entrainment of particles from the underthrust section (blue) in the base of the systems (Figure 3). Thus, substituting the residual friction angle of the wedge materials (12.5–14.0°; Table 3) for the décollement materials yields calculated surface slopes more consistent with those measured.

Technically, the occurrence of discrete faulting is inconsistent with critical wedge theory, because the system is not at failure throughout the wedge [*Davis et al.*, 1983], but only locally along the faults. Thus, the wedge does not grow in a self-similar fashion but instead goes through episodes of localized slip and thrust uplift on new or preexisting faults. As a result, the wedge geometry varies over time, and the critical taper is only an approximation [e.g., *Gutscher et al.*, 1996, 1998]. Nonetheless, the final wedge slopes fall within a narrow range, and the noncohesive Model A defines a reference wedge that most closely approximates the assumptions of critical Coulomb wedge theory.

Although the gross stress states of the wedges are predictable and consistent with previous observations and inferences, stress heterogeneities are clearly evident in the mapped stress fields and failure potential (Figures 6–9). Some of the heterogeneities are systematic; e.g., both τ_{\max} and σ_m increase with progressive tectonic loading (Figures 7, 8), and décollement propagation causes the progressive rotation of σ_i vectors (e.g., Figure 6). Other variations reflect differences in strength, for example, between coherent materials and the active faults that separate them. In addition, intermittent locking and release along the décollement, and the formation and slip of thrust faults, result in episodic changes in stress orientations and magnitudes during wedge growth, as captured for Model Y in the sequence leading up to the formation of T_4 (Figure 10). These latter heterogeneities play key roles in determining where and when the system will deform, but prove very difficult to constrain in natural systems, demonstrating the value of numerical simulations to parse them out.

Failure potential maps (Figure 9) offer a unique way to visualize the mechanical evolution and controls on faulting within the simulated wedges. These maps reveal where the stress conditions are most favorable for new faulting. The pronounced regions of high failure potential outboard of the deformation fronts reflect the extent of horizontal stress transmission, with widths increasing with material cohesion and correlating with increased thrust fault spacing (Figure 4). In contrast, the low failure potentials across much of the deformed wedges point to stress conditions below those necessary to generate brittle failure. At first order, this is due to the presence of preexisting faults, which now obey the residual sliding criterion (Figure 2), reducing the overall strength of the deformed wedge.

The cohesion of the shallow materials in these models may be exaggerated relative to natural systems, where strength will tend to increase with depth [*Jaeger and Cook*, 1979]. Real sedimentary sections typically consist of alternating weak and strong lithologies (e.g., shales versus sandstones and limestones), resulting in mechanical stratification that will tend to concentrate brittle deformation into particular layers, controlling the final fault geometries of the system [e.g., *Dahlstrom*, 1970; *Price*, 1981; *Boyer and Elliott*, 1982]. In such systems, the presence of strong layers well above the basal décollement may cause thrust faults to initiate within the section rather than rise from the décollement [e.g., *Kattenhorn and McConnell*, 1994; *McConnell et al.*, 1997], as has often been assumed based on noncohesive systems.

8.3. Stress Paths and Implications

The stress paths for elements tracked through the simulations (e.g., Figures 11 and 12) reveal direct connections between deformation and stress evolution, also strongly influenced by cohesive strength and

sample depth. Both décollement slip and thrusting play roles in the patterns of stress evolution, although the two modes of deformation are commonly out of phase (e.g., Figure 11). Episodes of décollement slip lead to the initial loading of the tracked elements, even well in front of the active deformation front. New or renewed thrust fault activity causes slip on the distal décollement to cease, freezing the stress state for an element far from the active fault. This results in the characteristic stepped stress paths prior to an element reaching its peak strength. The formation of a new fault at or near the tracked element results in a sudden drop in τ_{\max} , typically marking the peak strength of the element. In the shallower section, hanging wall elements maintain reduced values of τ_{\max} as they are carried up the fault; footwall elements will generally see further increases in τ_{\max} as they are buried beneath the growing wedge, potentially returning to values close to peak τ_{\max} . At greater depth, higher mean stresses and proximity to the active décollement result in more correlated stress paths, directly influenced by décollement slip events.

Local stress variations also occur in association with discrete deformation events within the wedge, in particular, during renewed fault or décollement slip. In the case of paired elements across a thrust fault, the stress changes can be positively or negatively correlated; the latter case is indicative of slip on a fault separating the elements. If stress changes are positively correlated, this reflects the response to more distal loading or unloading. The frequency of stress fluctuations tends to be greatest for the deeper elements, reflecting both the higher confining stress, and the proximity to the décollement, which exhibits stress perturbations during slip on the rough interface (e.g., Figure 10). The largest stress drops occur in association with thrust fault initiation, and can reach 10–20 MPa for the shallowest elements, decreasing with increasing depth. These magnitudes are comparable to typical stress drops associated with earthquakes, demonstrating a compelling match between models and nature.

The stress paths examined here compare nicely to the few sandbox experiments for which stresses have been estimated, also employing constant back wall displacements to induce contraction. Cruz *et al.* [2010] tracked the loads on the moving backstop necessary to maintain the backstop velocity, documenting distinct drops in the force that correlate directly with the formation and activity of forethrusts. Nieuwland *et al.* [2000] measured horizontal stresses at specific locations within the wedge, yielding stress paths that are similar to the differential stress paths shown here. Discrete sensors placed some distance from the moving back wall show stepped loading paths denoting distinct stress drops associated with forethrust formation, along with low-amplitude fluctuations between stress drops attributed to frictional slip along the faults. However, based on the models presented here, these fluctuations alternatively could be associated with décollement slip. In another case, three sensors are placed different distances from the back wall and tracked over time. Much like the stress paths shown for simulations A and F, the most proximal sensor initially shows greater signal than those farther away, although major changes associated with thrusting are correlated for all sensors. The highest signal and drop are recorded for the sensor closest to the final thrust to form, consistent with recording peak strength for the analog materials. Intriguingly, Nieuwland *et al.* [2000] also documents subtle density drops adjacent to the newly formed thrust fault, similar to the incremental dilation due to elastic rebound noted in Figure 5.

A comparison of the stress paths for the three representative simulations shown here reveals that higher-cohesive systems “feel” the effects of décollement slip much earlier than do low or noncohesive systems (Figures 11 and 12). The onset of loading for elements with similar initial positions occurs at Increment 70 for Model A, Increment 40 for Model F, and Increment 20 for Model Y. The loading rates for the three simulations, however, are not appreciably different. Thus, the time (or total back wall displacement) between onset of tectonic loading and when the peak strength is reached also increases with cohesion. This combination of conditions explains to first order the increase in spacing between thrust faults with increasing cohesion. In addition, the amount of precursory contractional strain is lower for high-cohesion materials (Figure 5), whereas the extent of décollement slip is greater (Figure 4). All of these phenomena are reflections of the greater ability of more cohesive materials to transmit stress across the model domain, without undergoing substantial internal deformation. Thus, interparticle bonds are supporting a greater proportion of the load in the high-cohesion materials compared to the lower-cohesion materials.

9. Conclusions

The simulations presented here demonstrate the power of particle-based modeling for exploring combined kinematic and mechanical processes in contractional systems. Material cohesion strongly influences the modes of deformation, ranging from comparatively distributed deformation in noncohesive systems to discrete imbricate thrusting in strong cohesive systems. Despite the differing modes of deformation, all of the simulations produced overall wedge geometries consistent with critical Coulomb wedges. In all systems, tectonic deformation is accompanied by substantial volume loss through horizontal contraction, a result of increased particle packing due to tectonic shortening. Faulting and local slip events are also accompanied by transient volume strains, primarily associated with elastic loading and unloading. Tectonically induced volumetric strain serves to strengthen the material, preconditioning it for brittle failure, specifically in the regions just outboard of the deformation front. New faults consistently initiate at shallow depths and propagate down toward the décollement.

All simulations exhibit heterogeneous stress distributions through time and space, controlled by material cohesion and deformation episodes. Failure potential, which scales stress ratios to the best fit failure criteria, documents the proximity to failure for a given system. Failure potential is highest in the unfaulted regions outboard of the deformation fronts in all wedges, where new faults will eventually break, and extends the farthest for the high-cohesion examples, which are best able to transmit stress. Once a new fault develops in this region, the local failure potential drops, reflecting the lower residual strength associated with slip on preexisting faults. Material elements tracked throughout the simulation demonstrate systematic variations in stress in response to episodes of décollement slip and thrust fault activity, experiencing both loading and unloading as a function of position relative to the deformation.

Forward modeling of this sort offers unique and fundamental insights into the mechanical evolution of tectonic systems. The ability to directly correlate transient physical and mechanical behaviors with observed deformation processes in contractional wedges is something that still cannot be done effectively in the laboratory or field, defining a unique tool for future study of tectonic systems.

Acknowledgments

This work was funded by National Science Foundation grant EAR-1145263 and support from ExxonMobil Corporation. Computing facilities were made available through the Rice Research Computing Support Group and the Rice Center for Computational Geophysics. The author benefitted from discussions about modeling, structural geology, and geomechanics with Oded Katz, Gary Gray, John Shaw, Tom Fournier, and others. The author is grateful for thoughtful reviews by Michele Cooke and an anonymous reviewer, which resulted in significant improvements in the manuscript. Modeling results and information can be obtained by contacting J. Morgan at morganj@rice.edu. Interested parties are encouraged to contact the author to request copies of animated GIFs of the simulations for further study.

References

- Adam, J., and C.-D. Reuther (2000), Crustal dynamics and active fault mechanics during subduction erosion: Application of frictional wedge analysis on to the North Chilean forearc, *Tectonophysics*, **321**, 297–325.
- Adam, J., J. L. Urai, B. Wieneke, O. Oncken, K. Pfeiffer, N. Kukowski, J. Lohrmann, S. Hoth, W. van der Zee, and J. Schmatz (2005), Shear localisation and strain distribution during tectonic faulting—New insights from granular-flow experiments and high-resolution optical image correlation techniques, *J. Struct. Geol.*, **27**, 283–301.
- Agarwal, K. K., and G. K. Agrawal (2002), Analogue sandbox models of thrust wedges with variable basal frictions, *Gondwana Res.*, **5**, 641–647.
- Aharanov, E., and D. Sparks (2004), Stick-slip motion in simulated granular layers, *J. Geophys. Res.*, **109**, B09306, doi:10.1029/2003JB002597.
- Bally, A. W., P. L. Gordy, and G. A. Steward (1966), Structure, seismic data, and orogenic evolution of the southern Canadian Rocky Mountains, *Bull. Can. Petrol. Geol.*, **14**, 337–381.
- Bigi, S., L. Di Paolo, L. Vadacca, and G. Gambardella (2010), Load and unload as interference factors on cyclical behavior and kinematics of Coulomb wedges: Insights from sandbox experiments, *J. Struct. Geol.*, **32**, 28–44.
- Bonini, M. (2007), Deformation patterns and structural vergence in brittle-ductile thrust wedges: An additional analogue modelling perspective, *J. Struct. Geol.*, **29**, 141–158.
- Bose, S., N. Mandal, D. K. Mukhopadhyay, and P. Mishra (2009), An unstable kinematic state of the Himalayan tectonic wedge: Evidence from experimental thrust-spacing patterns, *J. Struct. Geol.*, **31**, 83–91.
- Boyer, S. E., and D. Elliott (1982), Thrust systems, *AAPG Bull.*, **66**, 1196–1230.
- Bray, C. J., and D. E. Karig (1986), Porosity of sediments in accretionary prisms and some implications for dewatering processes, *J. Geophys. Res.*, **90**, 768–778, doi:10.1029/JB090iB01p00768.
- Buiter, S. J. H., A. Y. Babeyko, S. Ellis, T. V. Geryas, B. J. P. Kaus, A. Kellner, G. Schreurs, and Y. Yamada (2006), The numerical sandbox: Comparison of model results for a shortening and an extension experiment, in *Analogue and Numerical Modelling of Crustal-Scale Processes*, edited by S. J. H. Buiter and G. Schreurs, *Geol. Soc. London Spec. Publ.*, **253**, 29–64.
- Burbridge, D. R., and J. Braun (2002), Numerical models of the evolution of accretionary wedges and fold-and-thrust belts using the distinct-element method, *Geophys. J. Int.*, **148**, 542–561.
- Camac, B. A., S. P. Hunt, and P. J. Boult (2009), Predicting brittle cap-seal failure of petroleum traps: An application of 2D and 3D distinct element method, *Petrol. Geosci.*, **15**, 75–89, doi:10.1144/1354-079309-796.
- Chapple, W. M. (1978), Mechanics of thin-skinned fold-and-thrust belts, *Geol. Soc. Am. Bull.*, **113**, 443–453.
- Cooke, M. L., and E. H. Madden (2014), Is the Earth lazy? A review of work minimization in fault evolution, *J. Struct. Geol.*, **66**, 334–346.
- Costa, E., and B. C. Vendeville (2002), Experimental insights on the geometry and kinematics of fold-and-thrust belts above weak, viscous evaporitic décollement, *J. Struct. Geol.*, **24**, 1729–1739.
- Cotton, J. T., and H. A. Koyi (2000), Modeling of thrust fronts above ductile and frictional detachments: Application to structures in the Salt Range and Potward Plateau, Pakistan, *Geol. Soc. Am. Bull.*, **112**, 351–363.
- Couzens-Schultz, B. A., B. C. Vendeville, and D. Wiltschko (2003), Duplex style and triangle zone formation: Insights from physical modeling, *J. Struct. Geol.*, **25**, 1623–1644.

- Cruz, L., C. Teyssier, L. Perg, A. Take, and A. Fayon (2008), Deformation, exhumation, and topography of experimental doubly-vergent orogenic wedges subjected to asymmetric erosion, *J. Struct. Geol.*, 30, 98–115.
- Cruz, L., J. Malinski, A. Wilson, W. A. Take, and G. Hilley (2010), Erosional control of the kinematics and geometry of fold-and-thrust belts imaged in a physical and numerical sandbox, *J. Geophys. Res.*, 115, B09404, doi:10.1029/2010JB007472.
- Cubas, N., B. Maillot, and C. Barnes (2010), Statistical analysis of an experimental compressional sand wedge, *J. Struct. Geol.*, 32, 818–831.
- Cundall, P. A. (1987), Distinct element models of rock and soil structure, in *Analytical and Computational Methods in Engineering Rock Mechanics*, edited by E. T. Brown, pp. 129–163, Allen & Unwin, London.
- Cundall, P. A., and O. D. L. Strack (1979), A discrete numerical model for granular assemblies, *Geotechnique*, 29, 47–65.
- Cundall, P. A., and O. D. L. Strack (1983), Modeling of microscopic mechanisms in granular material, in *Mechanics of Granular Materials: New Models and Constitutive Relations*, edited by J. T. Jenkins and M. Satake, pp. 137–149, Elsevier Sci, New York.
- Dahlen, F. A. (1984), Non-cohesive critical Coulomb wedges: An exact solution, *J. Geophys. Res.*, 89, 10,125–10,133, doi:10.1029/JB089iB12p10125.
- Dahlen, F. A. (1990), Critical taper model of fold-and-thrust belts and accretionary wedges, *Ann. Rev. Earth Planet. Sci.*, 18, 55–99.
- Dahlen, F. A., J. Suppe, and D. Davis (1984), Mechanics of fold-and-thrust belts and accretionary wedges: Cohesive Coulomb theory, *J. Geophys. Res.*, 89, 10,087–10,101, doi:10.1029/JB089iB12p10087.
- Dahlstrom, C. D. A. (1970), Structural geology in the eastern margin of the Canadian Rocky Mountains, *Bull. Can. Petrol. Geol.*, 18, 332–406.
- Davis, D. M., and T. Engelder (1985), The role of salt in fold-and-thrust belts, *Tectonophysics*, 119, 67–88.
- Davis, D. M., J. Suppe, and F. A. Dahlen (1983), Mechanics of fold and thrust belts and accretionary wedges, *J. Geophys. Res.*, 88, 1,153–1,172, doi:10.1029/JB088iB02p01153.
- Dean, S., J. K. Morgan, and T. Fournier (2013), Geometries of frontal fold and thrust belts: Insights from discrete element simulations, *J. Struct. Geol.*, 53, 43–53.
- DeCelles, P. G., and G. Mitra (1995), History of the Sevier orogenic wedge in terms of critical taper models, northeast Utah and southwest Wyoming, *Geol. Soc. Am. Bull.*, 107, 454–462.
- Del Castello, M., and M. L. Cooke (2007), Underthrusting-accretion cycle: Work budget as revealed by the boundary element method, *J. Geophys. Res.*, 112, B12404, doi:10.1029/2007JB004997.
- Duerto, L., and K. McClay (2009), The role of syntectonic sedimentation in the evolution of double vergent thrust wedges and foreland folds, *Mar. Petrol. Geol.*, 26, 1051–1069.
- Egholm, D. L., M. Sandiford, O. R. Clausen, and S. B. Nielsen (2007), A new strategy for discrete element numerical models: 2. Sandbox applications, *J. Geophys. Res.*, 112, B05204, doi:10.1029/2006JB004558.
- Ferrill, D. A., and W. M. Dunne (1989), Cover deformation above a blind duplex: An example from West Virginia, U.S.A., *J. Struct. Geol.*, 11, 421–431.
- Fournier, T., and J. K. Morgan (2012), Insights to slip behavior on rough faults using discrete element modeling, *Geophys. Res. Lett.*, 39, L12304, doi:10.1029/2012GL051899.
- Frye, F. M., and C. Marone (2002), The effect of particle dimensionality on granular friction in laboratory shear zones, *Geophys. Res. Lett.*, 29, 1916, doi:10.1029/2002GL015709.
- Gray, G. G., J. K. Morgan, and P. F. Sanz (2014), Strategies, methods, and pitfalls in numerical modeling of geologic structures, *J. Struct. Geol.*, 59, 19–36.
- Guo, Y., and J. K. Morgan (2007), Fault gouge evolution and its dependence on normal stress and rock strength—Results of discrete element simulations: Gouge zone properties, *J. Geophys. Res.*, 112, B10403, doi:10.1029/2006JB004524.
- Guo, Y., and J. K. Morgan (2008), Fault gouge evolution and its dependence on normal stress and rock strength—Results of discrete element simulations: Gouge zone micromechanics, *J. Geophys. Res.*, 113, B08417, doi:10.1029/2006JB004525.
- Gutscher, M. A., N. Kukowski, J. Malavieille, and S. Lallemand (1996), Cyclical behavior of thrust wedges: Insights from high basal friction sandbox experiments, *Geology*, 24, 135–138.
- Gutscher, M. A., N. Kukowski, J. Malavieille, and S. Lallemand (1998), Material transfer in accretionary wedges from analysis of a systematic series of analog experiments, *J. Struct. Geol.*, 20, 407–416.
- Hafner, W. (1951), Stress distributions and faulting, *Geol. Soc. Am. Bull.*, 62, 373–398.
- Hardy, S., K. McClay, and J. A. Munoz (2009), Deformation and fault activity in space and time in high-resolution numerical models of doubly vergent thrust wedges, *Mar. Pet. Geol.*, 26, 232–248.
- Hoshino, K., H. Koide, K. Inami, S. Iwamura, and S. Mitsui (1972), Mechanical properties of Japanese Tertiary sedimentary rocks, Rep. 244, Geol. Surv. Jpn., Kawasaki, 200 pp.
- Itasca Consulting Group (1999), *PFC2D (Particle Flow Code in 2 Dimensions)*, Itasca Consulting Group, Minneapolis, Minn.
- Jaeger, J. C., and N. G. W. Cook (1979), *Fundamentals of Rock Mechanics*, 379 pp., Chapman and Hall.
- Johnson, K. L. (1985), *Contact Mechanics*, Cambridge Univ. Press, Cambridge.
- Kattenhorn, S. A., and D. A. McConnell (1994), Analysis of outcrop-scale fault-related folds, Eagle Rock, Virginia, *Southeast. Geol.*, 34, 79–88.
- Katz, O., J. K. Morgan, E. Aharanov, and B. Dugan (2014), Controls on the geometry and size of landslides: Insights from DEM computer simulations, *Geomorphology*, 220, 104–113.
- Konstantinovskaya, E., and J. Malavieille (2011), Thrust wedges with décollement levels and syntectonic erosion: A view from analog models, *Tectonophysics*, 502, 336–350.
- Konstantinovskaya, E., D. Rodriguez, D. Kirkwood, L. B. Harris, and R. Theriault (2009), Effects of basement structure, sedimentation and erosion on thrust wedge geometry: An example from the Quebec Appalachians and analogue models, *Bull. Can. Petrol. Geol.*, 57, 34–62.
- Koyi, H. (1995), Mode of internal deformation in sand wedges, *J. Struct. Geol.*, 17, 293–300.
- Koyi, H. A., M. Sans, A. Teixell, J. Cotton, and H. Zeyen (2004), The significance of penetrative strain in the restoration of shortened layers—Insights from sand models and the Spanish Pyrenees, in *Thrust Tectonics and Hydrocarbon Systems*, AAPG Mem., vol. 82, edited by K. R. McClay, pp. 207–222, Tulsa, Okla.
- Koyi, H., and B. C. Vendeville (2003), The effect of décollement dip on geometry and kinematics of model accretionary wedges, *J. Struct. Geol.*, 25, 1445–1450.
- Lallemand, S. E., P. Schnurle, and J. Malavieille (1994), Coulomb theory applied to accretionary and non-accretionary wedges: Possible causes for tectonic erosion and/or frontal accretion, *J. Geophys. Res.*, 99, 12,033–12,055, doi:10.1029/94JB00124.
- Lohrmann, J., N. Kukowski, J. Adam, and O. Oncken (2005), The impact of analogue material properties on the geometry, kinematics, and dynamics of convergent sand wedges, *J. Struct. Geol.*, 25, 1691–1711.
- Lujan, M., F. Storti, J.-C. Balanya, A. Crespo-Blanc, and F. Rossetti (2003), Role of décollement material with different rheological properties in the structure of the Aljibe thrust imbricate (Flysch Trough, Gibraltar Arc): An analogue modelling approach, *J. Struct. Geol.*, 25, 867–881.

- Mair, K., K. Frye, and C. J. Marone (2002), Influence of grain characteristics on the friction of granular shear zones, *J. Geophys. Res.*, 107(10), 2219, doi:10.1029/2001JB000516.
- Malvern, L. E. (1969), *Introduction to the Mechanics of a Continuous Medium*, Prentice-Hall, Englewood Cliffs, N. J.
- Mandl, G. (1988), *Mechanics of Tectonic Faulting*, 407 pp., Elsevier, Amsterdam.
- Mandal, N., A. Chattopadhyay, and S. Bose (1997), Imbricate thrust spacing: Experimental and theoretical analyses, in *Evolution of Geological Structures in Macro- to Micro-Scales*, edited by S. Sengupta, pp. 143–165, Chapman and Hall, London.
- Marshak, S., and M. S. Wilkerson (1992), Effect of overburden thickness on thrust belt geometry and development, *Tectonics*, 11, 560–566, doi:10.1029/92TC00175.
- McConnell, D., S. A. Kattenhorn, and L. M. Benner (1997), Distribution of fault slip in outcrop-scale fault-related folds, Appalachian Mountains, *J. Struct. Geol.*, 19, 257–267.
- McGovern, P. J., and J. K. Morgan (2009), Volcanic spreading and lateral variations in the structure of Olympus Mons, Mars, *Geology*, 37, 139–142, doi:10.1130/G25180A.1.
- Mitra, G. (1997), Evolution of salients in a fold-and-thrust belt: The effects of sedimentary basin geometry, strain distribution and critical taper, in *Evolution of Geological Structures in Micro- to Macro-Scales*, edited by S. Sengupta, pp. 59–90, Chapman and Hall, London.
- Miyakawa, A., Y. Yamada, and T. Matsuoka (2010), Effect of increased shear stress along a plate boundary fault on the formation of an out-of-sequence thrust and break in surface slope within an accretionary wedge based on numerical simulations, *Tectonophysics*, 484, 127–138.
- Mora, P., and D. Place (1993), A lattice solid model for the non-linear dynamics of earthquakes, *Int. J. Mod. Phys. C*, 4, 1059–1074.
- Morgan, J. K. (1999), Numerical simulations of granular shear zones using the distinct element method: II. The effect of particle size distribution and interparticle friction on mechanical behavior, *J. Geophys. Res.*, 104, 2721–2732, doi:10.1029/1998JB900055.
- Morgan, J. K. (2004), Particle dynamics simulations of rate and state dependent frictional sliding of granular fault gouge, *Pure Appl. Geophys.*, 161, 1877–1891.
- Morgan, J. K., and M. S. Boettcher (1999), Numerical simulations of granular shear zones using the distinct element method: I. Shear zone kinematics and micromechanics of localization, *J. Geophys. Res.*, 104, 2703–2719, doi:10.1029/1998JB900056.
- Morgan, J. K., and P. J. McGovern (2005a), Discrete element simulations of gravitational volcanic deformation: 1. Deformation structures and geometries, *J. Geophys. Res.*, 110, B05402, doi:10.1029/2004JB003252.
- Morgan, J. K., and P. J. McGovern (2005b), Discrete element simulations of gravitational volcanic deformation: 2. Mechanical analysis, *J. Geophys. Res.*, 110, B05403, doi:10.1029/2004JB003253.
- Morgan, J. K., D. E. Karig, and A. Maniatty (1994), The estimation of diffuse strains in the toe of the Nankai accretionary prism: A kinematic solution, *J. Geophys. Res.*, 99, 7019–7032, doi:10.1029/93JB03367.
- Muir Wood, D. (1990), *Soil Behaviour and Critical State Soil Mechanics*, 462 pp., Cambridge Univ. Press, New York.
- Mulugeta, G. (1988), Modelling the geometry of Coulomb thrust wedges, *J. Struct. Geol.*, 10, 847–859.
- Mulugeta, G., and H. Koyi (1987), Three-dimensional geometry and kinematics of experimental piggyback thrusting, *Geology*, 15, 1052–1056.
- Naylor, M., H. D. Sinclair, S. Willett, and P. A. Cowie (2005), A discrete element model for orogenesis and accretionary wedge growth, *J. Geophys. Res.*, 110, B12403, doi:10.1029/2003JB002940.
- Nieuwland, D. A., J. L. Urai, and M. Knoop (2000), In-situ stress measurements in model experiments of tectonic faulting, in *Aspects of Tectonic Faulting*, edited by F. K. Lehner and J. L. Urai, pp. 155–166, Springer, Berlin.
- Nilforoushan, F., H. A. Koyi, J. O. H. Swantesson, and C. J. Talbot (2008), Effect of basal friction on surface and volumetric strain in models of convergent settings measured by laser scanner, *J. Struct. Geol.*, 30, 366–379.
- Oda, M., and K. Iwashita (1990), *Mechanics of Granular Materials: An Introduction*, A.A. Balkema, Rotterdam.
- Onasch, C. M. (1994), Assessing brittle volume-gain and pressure solution volume-loss processes in quartz arenite, *J. Struct. Geol.*, 16, 519–530.
- Potyondy, D. O., and P. A. Cundall (2004), A bonded-particle model for rock, *Int. J. Rock Mech. Mining Sci.*, 41, 1329–1364.
- Price, R. A. (1981), The Cordilleran foreland thrust and fold belt in the southern Canadian Rocky Mountains, in *Thrust and Nappe Tectonics*, edited by K. R. McClay and N. J. Price, *Geol. Soc. London Spec. Publ.*, 9, 427–448.
- Ruh, J. B., B. J. P. Kaus, and J.-P. Burg (2012), Numerical investigation of deformation mechanics in fold-and-thrust belts: Influence of rheology of single and multiple décollements, *Tectonics*, 31, TC3005, doi:10.1029/2011TC003047.
- Sanz, P. F., D. D. Pollard, P. F. Allwardt, and R. I. Borja (2008), Mechanical models of fracture reactivation and slip on bedding surfaces during folding of the asymmetric anticline at Sheep Mountain, Wyoming, *J. Struct. Geol.*, 30, 1177–1191.
- Schellart, W. P. (2000), Shear test results for cohesion and friction coefficients for different granular materials: Scaling implications for their usage in analogue modelling, *Tectonophysics*, 324, 1–16.
- Scholz, C. H. (1990), *The Mechanics of Earthquakes and Faulting*, Cambridge Univ. Press, New York.
- Schöpfer, M. P. J., C. Childs, and J. J. Walsh (2007a), Two-dimensional distinct element modeling of the structure and growth of normal faults in multilayer sequences: 1. Model calibration, boundary conditions, and selected results, *J. Geophys. Res.*, 112, B10401, doi:10.1029/2006JB004902.
- Schöpfer, M. P. J., C. Childs, and J. J. Walsh (2007b), Two-dimensional distinct element modeling of the structure and growth of normal faults in multilayer sequences: 2. Impact of confining pressure and strength contrast on fault zone geometry and growth, and selected results, *J. Geophys. Res.*, 112, B10404, doi:10.1029/2006JB004903.
- Schöpfer, M. P. J., C. Childs, and T. Manzocchi (2013), Three-dimensional failure envelopes and the brittle-ductile transition, *J. Geophys. Res. Solid Earth*, 118, 1378–1392, doi:10.1002/jgrb.50081.
- Schott, B., and H. A. Koyi (2001), Estimating basal friction in accretionary wedges from the geometry and spacing of frontal faults, *Earth Planet. Sci. Lett.*, 194, 221–227.
- Schreurs, G., et al. (2006), Analogue benchmarks of shortening and extension experiments, in *Analogue and Numerical Modeling of Crustal-Scale Processes*, edited by S. Buitter and G. Schruers, *Geol. Soc. London Spec. Publ.*, 253, 1–27.
- Schumann, K., J. H. Behrmann, M. Stipp, Y. Yamamoto, Y. Kitamura, and C. Lempp (2014), Geotechnical behavior of mudstones from the Shimanto and Boso accretionary complexes, and implications for the Nankai accretionary prism, *Earth Planets Space*, 66, doi:10.1186/1880-5981-66-129.
- Simpson, G. (2011), Mechanics of non-critical fold-thrust belts based on finite element models, *Tectonophysics*, 499, 142–155.
- Souloumiac, P. K., Y. M. Leroy, B. Maillot, and K. Krabbenhoft (2009), Predicting stress distributions in fold-and-thrust belts and accretionary wedges by optimization, *J. Geophys. Res.*, 114, B09404, doi:10.1029/2008JB005986.
- Souloumiac, P., K. Krabbenhoft, Y. M. Leroy, and B. Maillot (2010), Failure in accretionary wedges with the maximum strength theorem: Numerical algorithm and 2D validation, *Comput. Geosci.*, 14, 793–811.

- Stockmal, G., C. Beaumont, M. Nguyen, and B. Lee (2007), Mechanics of thin-skinned fold-thrust belts: Insights from numerical models, in *Whence the Mountains: Inquiries into the Evolution of Orogenic Systems: A Volume in Honor of Raymond A. Price*, Geol. Soc. Am. Spec. Pap., vol. 433, edited by J. Sears, T. Harms, and C. Evenchick, pp. 63–98, Boulder, Colo.
- Strayer, L. M., S. G. Erickson, and J. Suppe (2004), Influence of growth strata on the evolution of fault-related folds—Distinct-element models, in *Thrust Tectonics and Hydrocarbon Systems*, Am. Assoc. Petrol. Geol. Mem., vol. 82, edited by K. R. McClay, pp. 413–437, Tulsa, Okla.
- Teixell, A., and H. A. Koyi (2003), Experimental and field study of the effects of lithological contrasts on thrust-related deformation, *Tectonics*, 22(5), 1054, doi:10.1029/2002TC001407.
- Thornton, C., and D. J. Barnes (1986), Computer simulated deformation of compact granular assemblages, *Acta Mech.*, 64, 45–61.
- Vidal-Royo, H. K., and J. A. Munoz (2009), Formation of orogen-perpendicular thrusts due to mechanical contrasts in the basal décollement in the Central External Sierras (Southern Pyrenees, Spain), *J. Struct. Geol.*, 31, 523–539.
- Vietor, T. (2003), Numerical simulation of collisional orogeny using the distinct element technique, in *Numerical Modeling in Micromechanics via Particle Methods*, edited by S. Konietzky and L. Zeitinger, pp. 295–301, A.A. Balkema, Lisse, Netherlands.
- Walton, O. R. (1995), Force models for particle-dynamics simulations of granular materials, in *Mobil Particulate Systems*, edited by E. Guazzelli and L. Oger, pp. 366–378, Kluwer Acad., Dordrecht, Netherlands.
- Wessel, P., and W. H. F. Smith (1995), *The Generic Mapping Tools (GMT) Version 3.0, Technical Reference & Cookbook*, Sch. of Ocean and Earth Sci. and Technol., Honolulu, Hawaii.
- Willet, S. (1999), Orogeny and orography: The effects of erosion on the structure of mountain belts, *J. Geophys. Res.*, 104, 28,957–28,981, doi:10.1029/1999JB900248.
- Yamada, Y., and T. Matsuoka (2005), Digital sandbox modeling using distinct element method: Applications to fault tectonics, in *Faults, Fluid Flow, and Petroleum Traps*, Am. Assoc. Petrol. Geol. Mem., vol. 85, edited by R. Sorkhabi and Y. Tsuji, pp. 107–123, Tulsa, Okla.
- Yamada, Y., K. Baba, and T. Matsuoka (2006), Analogue and numerical modeling of accretionary prisms with a décollement in sediments, in *Analogue and Numerical Modelling of Crustal-Scale Processes*, edited by S. J. H. Buiter and G. Schruers, *Geol. Soc. London Spec. Publ.*, 253, 169–183.
- Zhang, J., J. K. Morgan, G. G. Gray, N. W. Harkins, P. F. Sanz, and I. Chikichev (2013), Comparative FEM and DEM modeling of basement-involved thrust structures, with application to Sheep Mountain, Greybull area, Wyoming, *Tectonophysics*, 608, 408–417.
- Zhao, W.-L., D. M. Davis, F. A. Dahlen, and J. Suppe (1986), Origin of convex accretionary wedges: Evidence from Barbados, *J. Geophys. Res.*, 91, 10,246–10,258, doi:10.1029/JB091B10p10246.